Research Square

Preprints are preliminary reports that have not undergone peer review.
They should not be considered conclusive, used to inform clinical practice,
or referenced by the media as validated information.

Transient reduction of neuronal electrical activity replenishes energy levels and protects PARK2 patient- derived neurons against oxidative stress

Bridget Milky
South Australian Health and Medical Research Institute (SAHMRI)
Robert Adams
South Australian Health and Medical Research Institute (SAHMRI)
Paris Mazzachi
Flinders University
Amal Abdirashid Ali
Flinders University
Imanthi Illeperuma
Flinders University
Tim Sargeant
The University of Adelaide
Cedric Bardy
cedric.bardy@sahmri.com

Flinders University

Article

Keywords: Ion channel modulators, Optogenetics, Halorhodopsin, Neurometabolism, Neuroprotection, Cell repair, Human neurons, iPSC, Stem cells, Midbrain, Substantia nigra, Dopaminergic neurons, Parkinson's disease, Electrophysiology, Neurodegeneration, PARK2, Parkin

Posted Date: September 18th, 2026

DOI: https://doi.org/10.21203/rs.3.rs-10696877/v1

License: This work is licensed under a Creative Commons Attribution 4.0 International License.
Read Full License

Additional Declarations: No competing interests reported.

Transient reduction of neuronal electrical activity replenishes energy levels and protects PARK2 patient-derived neurons against oxidative stress

Bridget Milky[1,2,#], Robert Adams[1,2,#], Paris Mazzachi[1,2], Amal Abdirashid Ali[1,2], Imanthi Illeperuma[1,2], Tim Sargeant[3,4], Cedric Bardy[1,2]*

Affiliations:
1. Laboratory for Human Neurobiology, South Australian Health and Medical Research Institute (SAHMRI), Adelaide, South Australia, Australia
2. Flinders Health and Medical Research Institute, College of Medicine and Public Health, Flinders University, Adelaide, South Australia, Australia
3. Lysosome Health in Ageing laboratory, Hopwood Centre for Neurobiology, SAHMRI, Adelaide, South Australia, Australia
4. Faculty of Health and Medical Sciences, The University of Adelaide, Adelaide, SA, Australia

# Equal contributions
*Lead correspondence: cedric.bardy@sahmri.com

Short title: Ion channel modulators raise ATP levels and provide neuroprotection

Keywords:
Ion channel modulators; Optogenetics; Halorhodopsin; Neurometabolism; Neuroprotection; Cell repair; Human neurons; iPSC; Stem cells; Midbrain; Substantia nigra; Dopaminergic neurons; Parkinson's disease; Electrophysiology; Neurodegeneration; PARK2; Parkin

ABSTRACT (166 words):
Ageing-associated metabolic decline compromises neuronal repair and accelerates neurodegeneration, yet strategies to restore neuronal energy balance remain limited. Here, we show in human neural cultures that pharmacological or optogenetic inhibition of neuron electrical activity raises their ATP levels, or replenishes them during mild mitochondrial impairment. Transiently reducing neuron electrical activity enhances lysosomal function and protects from oxidative toxicity. To test relevance to Parkinson's disease (PD), we identify targetable ion channel subunits enriched in vulnerable substantia nigra dopaminergic neurons. Modulating these channels, including inwardly rectifying potassium channels, nicotinic acetylcholine receptors, and cyclic nucleotide-gated cation channels, increases ATP in human substantia nigra-patterned cultures. PD patient-derived and CRISPR-engineered *PARK2*-mutant dopaminergic neurons exhibit heightened oxidative-stress vulnerability, which is reduced by modulating the activity of broadly expressed voltage-gated sodium channels as well as more substantia nigra-specific channels. These findings identify neuronal electrical activity modulation as a neuroprotective mechanism and support its further preclinical investigation as a complementary and tunable strategy to mitigate bioenergetic stress in neurodegenerative disorders.

SIGNIFICANCE STATEMENT (117 words)
Neurons devote substantial energy to ion channel activity and synaptic transmission, making them especially vulnerable to metabolic stress. When energy is limited or neuronal activity is abnormally high, prioritising electrical activity and neurotransmission can compromise other essential energy-dependent maintenance pathways, thereby accelerating neurodegeneration. Whether neuronal energy can be partially redirected away from excessive electrical activity to enhance repair and resilience has remained unclear. Here, we show, using multiple complementary approaches, that lowering electrical activity increases ATP availability and protects human neurons against oxidative stress and genetic metabolic vulnerability in Parkinson's disease. These findings identify activity-dependent energy reallocation as a neuroprotective mechanism and provide preliminary preclinical support for an alternative therapeutic strategy to mitigate metabolic stress in neurodegenerative disorders.

INTRODUCTION

Enhancing neuronal metabolism is emerging as an attractive strategy to improve brain health and resilience to age-related neurological disease[1,2]. Cellular metabolism declines with age, creating energetic stress that can disproportionately affect neurons because of their high and sustained energy requirements[3]. Disrupted metabolism is also increasingly implicated in the onset and progression of neurological disorders[4], including Parkinson's disease (PD)[5,6], Alzheimer's disease[7], and Amyotrophic Lateral Sclerosis[8]. Across these conditions, neurons exhibit alterations in key metabolic pathways, including mitochondrial and mitophagy dysfunction, dysregulated glucose metabolism, and increased oxidative stress[1,9,10]. They can arise from mutations in genes that regulate mitochondrial quality control and stress responses, for example, *PARK2*, *PINK1*, and *PARK7*, which are associated with familial forms of PD [11]. These metabolic deficits can act both as causes and consequences of other disease-associated processes, such as proteopathy[12,13], redox imbalance[14-16], and synaptic failure[12,17-19]. Reduced ATP availability can compromise energy-dependent neuroprotective pathways, including proteostasis, autophagy–lysosomal function, antioxidant defence, and cellular repair [20,21]. Restoring or preserving neuronal energetics could therefore enhance cellular maintenance mechanisms and promote the return to homeostasis. Consistent with this idea, enhancing glycolysis through activation of phosphoglycerate kinase 1 (PGK1), which increases neuronal energy availability, has been associated with reduced PD risk in men[2,22]. However, despite these promising associations, there are currently no approved clinical treatments that halt neurodegeneration by directly restoring neuronal energetics, and further preclinical research is needed.

In PD, degeneration of dopaminergic (DA) neurons of the substantia nigra pars compacta (SNpc) is closely associated with energetic stress[6,23]. PD symptoms arise when a substantial number of dopaminergic neurons in the SNpc are lost (>70%). This cell loss increases the electrical demand on the remaining neurons, which must compensate to maintain midbrain function[24-26]. A substantial proportion of neuronal ATP consumption supports electrical and synaptic processes required for neuronal communication[27-30]. SNpc dopaminergic neurons must propagate signals across distant brain regions and through more synapses than most other neuronal types[31], suggesting greater relative ATP needs. Furthermore, SNpc dopaminergic neurons exhibit autonomous pacemaking and high-frequency bursting activity, which impose a substantial metabolic cost[32-35]. Their pacemaking activity is associated with large Ca^{2+} oscillations, while their lack of calbindin compared with more resilient dopaminergic populations may further limit their capacity to buffer calcium-dependent mitochondrial stress when workloads increase[36,37]. Together, these unique features are thought to constrain spare energy capacity, rendering them particularly vulnerable in the context of ageing and neurodegeneration[26,31,38-41]. In addition, genetic mutations and exposure to external toxins that impair mitochondrial function significantly increase Parkinson's disease prevalence[11,42-44]. These observations support a model in which sustained activity-dependent energy demand competes with essential ATP-dependent maintenance pathways, including autophagy, proteostasis and molecular repair. Under conditions of mitochondrial impairment or oxidative stress, this imbalance may create a vicious cycle that accelerates neuronal dysfunction and degeneration.

Developing therapeutics that improve neuronal bioenergetic resilience remains an important medical challenge. We propose an alternative and complementary strategy: reprioritising limited ATP reserves towards neuroprotection by transiently lowering excessive energetic demands for neuronal electrical activity. Here, we evaluate the potential merit of this strategy in a preclinical model, using human pluripotent stem cell (hPSC)-derived midbrain neural cultures. We found that reducing electrical activity increases ATP availability, particularly when mitochondrial oxidative phosphorylation is impaired. This increased energy availability was associated with improved ATP-dependent cellular functions, including lysosomal activity, and with protection against oxidative stress-induced toxicity. We tested our hypothesis using two independent approaches to reduce electrical activity: ion channel modulators (ICMs) and optogenetic inhibition (halorhodopsin). We also identified ion channel subunits enriched in human SNpc dopaminergic neurons, a population selectively vulnerable in PD. Targeting these channels with a combination of ICMs provided a means to transiently reduce neuronal activity and increase ATP reserves.

Finally, we tested the effect of ICMs using patient-derived induced pluripotent stem cells (iPSCs) harbouring distinct *PARK2* loss-of-function mutations, and an isogenic iPSC pair carrying a CRISPR-engineered *PARK2* mutation. We found that *PARK2*-mutant neurons are more sensitive to oxidative and dopaminergic stress than healthy neurons, and ICM treatment conferred neuroprotection. These results suggest that transient periods of reduced neuronal electrical activity may preserve neuronal health by relieving energetic stress, supporting further investigation of activity modulation as a potential neuroprotective strategy in PD and related neurodegenerative disorders.

RESULTS

Generation of functional human midbrain neural cultures enriched for substantia nigra neurons.

Action potential firing, propagation and synaptic communication are major consumers of neuronal energy[27,28]. To investigate how neuronal electrical activity modulation may alter energy levels, we first developed a model of functionally active neurons with high energy use. For this, we generated midbrain neural cultures enriched for substantia nigra features from human stem cells (**Figure 1A**), maintained in BrainPhys neuronal medium for optimal neurophysiological maturation[45,46]. To confirm neuronal identity, we assessed midbrain region specificity. Neurons of the SNpc are predisposed to degeneration in PD and are identifiable by their expression of GIRK2 (A9 region) but not Calbindin (A10 region). Over 80% of our hPSC-derived neurons (MAP2+) exclusively expressed GIRK2 (**Figure 1B**). Furthermore, the transcription factors LMX1A and FOXA2 are active during the specification of dopaminergic neurons. Approximately 80% of neurons expressed both LMX1A and FOXA2, and 25% expressed tyrosine hydroxylase (TH), confirming the enrichment of substantia nigra features in our neural model, consistent with hiPSC-derived dopaminergic models in the field[11]. Dopaminergic neurons act as neuromodulators of excitation and inhibition in the brain. Therefore, our human midbrain model also includes excitatory and inhibitory neurons, as well as astrocytes, to replicate physiologically relevant neural circuits [45-50].

We confirmed the emergence of functional and synchronous neuronal activity using multi-electrode arrays (MEA) for population-level electrophysiology (**Figure 1C**) and whole-cell patch-clamping for single-cell neurophysiological characterisation (**Figure 1D-F**). Over time, the neural cultures became increasingly active, with more neurons spontaneously firing action potentials at increasingly higher firing rates (**Figure 1C**). Firing patterns matured into synchronous networks as early as ~40 days in culture, demonstrating the presence of functional synaptic connections between neurons. Using whole-cell patch-clamp recordings, we further characterised the functional maturity of individual neurons in these cultures. Of 70 neurons recorded, >90% displayed repetitive firing properties, with the large majority firing at >10Hz (Type 5 [47])(**Figure 1D**). The neurons also displayed large voltage-gated sodium and potassium channels (**Figure 1E**), as well as functional excitatory and inhibitory synapses (**Figure 1F**). Together, these data validate the development of human midbrain neural cultures that are electrically active, synaptically connected, and contain dopaminergic neurons, forming a neural network physiologically relevant to this study.

Transient blocking of neuronal electrical activity by generic ion channel modulators raises ATP levels.

Having established electrically active and synaptically functional midbrain neural cultures enriched for dopaminergic features, we exposed them to a combination of ion channel modulators (ICMs; Table 1) to broadly block voltage-gated sodium channels and excitatory receptors (AMPA/NMDA). We measured culture ATP levels and metabolism to determine if blocking electrical activity raises neuronal energy levels and increases spare respiratory capacity (**Figures 2A, 2C and 2J**). The ICM combination reversibly silenced all action potential firing (**Figure 2B**). 24-hour exposure to the ICM combination resulted in a 75% increase in culture ATP levels compared to the control cultures (**Figure 2D**). ICM exposure produced a non-significant trend towards decreased ATP production through both mitochondrial and glycolytic pathways (**Figures 2E-F**), without a significant shift in mitochondria/glycolytic proportional contributions (**Figure 2G**). ICM exposure also significantly increased spare respiratory capacity by ~55% over the controls, a consequence of significantly decreased basal respiration with no change to maximum respiration rate (**Figure 2H** and **Supplementary Figure S1A**). Coupling efficiency of oxygen consumption to ATP production was unaltered by ICM exposure, indicating that ICMs were not impairing the electron transport chain (**Figure 2I**). These results indicate that blocking neuronal electrical activity both raises available cellular ATP levels and increases the ATP-producing reserve capacity that could be used to buffer against higher levels of ATP consumption and energetic stress.

To mimic decreased energy levels implicated in PD and ageing, neural cultures were exposed to rotenone, an inhibitor of mitochondrial complex I often used to establish rodent models of PD[51]. For each set of independent experiments, we determined the rotenone concentration that reduced neuronal ATP levels by approximately 50% (IC50; averaged data in Supplementary Figure S1B). At these concentrations, rotenone did not cause detectable neurodegeneration but reduced neuronal firing rates (**Supplementary Figure**

S1C,D), consistent with impaired maintenance of neuronal electrical activity under energetic stress **(Supplementary Figures S1B–D and S2C**). As such, rotenone modelled a state of mitochondrial energetic stress indirectly accompanied by some functional suppression, rather than selective degeneration of one cellular subtype. ICM exposure restored ATP levels in cultures exposed to rotenone (**Figure 2K**). In a preliminary cortical-patterned neural culture experiment, ICMs also increased ATP levels in rotenone-exposed cultures, suggesting that this effect may not be restricted to midbrain cultures (**Supplementary Figure S1E-H**). As expected of the mitochondrial toxin, rotenone exposure significantly decreased mitochondrial ATP production rates by ~66% compared to the control (**Figure 2L**). However, while it did not significantly increase glycolytic ATP production rates, it did significantly alter the ratio of glycolysis to oxidative phosphorylation (**Figure 2M-N**). ICM treatment did not rescue the changes to mitochondrial ATP production rates or the mitochondrial:glycolytic ATP production ratio. Instead, ICM treatment raised the neuronal spare respiratory capacity by 75% despite rotenone's presence (**Figure 2O**). Rotenone significantly reduced the mitochondrial coupling efficiency, which ICM treatment rescued (**Figure 2P**). Reductions in coupling efficiency indicate dysfunctional mitochondria, consuming oxygen without effective oxidative phosphorylation. Therefore, this result suggests that blocking neuronal electrical activity improves bioenergetic efficiency in addition to raising available ATP levels.

Optogenetic inhibition of neuronal electrical activity restores ATP levels in midbrain neurons with impaired mitochondria.

Optogenetics provides an optically controlled method for modulating neuronal activity via light-gated ion channels without ion channel-modulating compounds. We used the light-activated chloride channel halorhodopsin (eNpHR 3.0; **Figure 3A**) to inhibit neuronal firing rates and further confirm, with an independent method, that the increased ATP level observed after ICM exposure indeed resulted from lowering electrical activity. When stimulated with yellow light, membrane-bound halorhodopsin pumps chloride ions into the neuron to cause hyperpolarisation and subsequent inhibition of action potentials (**Supplementary Figure S2A)**. Cultures were optically stimulated by 594 nm light using a Lumos LED controller or custom-built LAVA board with a 3-minute-on 3-minute-off repeating pattern. The off period was necessary to prevent overheating during extended treatment periods. Short-term (3 minutes) optical stimulation reversibly decreased neuronal firing rates by 60% (**Figure 3B, Supplementary Figure S2B**), while the repeating pattern over 24 hours stably and reversibly decreased average firing rates by 25-50% (**Figure 3C**). The 24-hour exposure window was chosen to match the 24-hour rotenone and ICM treatment paradigm. Opto-inhibited neurons exhibited restored firing rates just over 36 hours after treatment finished, a much shorter period of time than it took TTX-treated neurons to recover (**Figure 2B**), likely due to kinetic and temporal differences between compound-mediated suppression and light-activated opsins.

To investigate whether optogenetic-mediated reduction in neuronal firing rates can restore ATP levels in the presence of mitochondrial dysfunction, halorhodopsin-expressing neurons were exposed to rotenone and the opto-inhibition stimulation pattern for 24 hours (**Figure 3D**). The opto-inhibition mitigated the rotenone-induced reduction in both numbers of active neurons and neuronal firing rates (**Supplementary Figure S2C**). Similar to the effects of the ICM cocktail, lowering neuronal electrical activity via opto-inhibition increased neuronal ATP levels by 50%, and fully restored them in cultures co-exposed to rotenone (**Figures 3E-F**).

To cope with acute and unpredictable changes in energy demand in functional neurons, non-canonical mechanisms involving Na+ pumps can tightly regulate ATP levels and maintain neuronal energy homeostasis[52]. The ICM cocktail we used targets multiple Na+ channels. However, the similar increase in neuronal ATP levels observed with halorhodopsin, a light-gated chloride pump, suggests that this energetic enhancement is not directly reliant on drug interactions with Na^+ pumps but rather depends more broadly on reduced firing activity. With two independent methods, we have shown that partial reductions of electrical activity can substantially raise neuronal ATP levels, particularly in the context of mitochondrial impairment.

Ion channels with higher expression in human midbrain SN neurons.

The ICM cocktail consists of broad-spectrum neurotoxins (TTX, NBQX, APV) that will indiscriminately block the activity of all neurons regardless of subtype and brain region. However, some ion channels display heterogeneous expression throughout the brain, with differences in expression found across brain regions and between neuronal subtypes. By modulating only target neurons of interest with highly specific ion channel modulators, we may be able to avoid undesirable broad and nonspecific neuronal silencing. Here we aimed to identify ion channels uniquely or preferentially expressed by neurons within the substantia nigra relative to other brain regions and other regions of the body using bulk RNA-sequencing data from the Gene Tissue Expression (GTEx) project (**Figure 4A**). Differential expression analysis of GTEx data comparing the SN to other regions of the brain revealed several ion channels significantly upregulated in the SN, eight of which we chose to pursue for electrical activity modulation potential (**Figure 4B,** P2RX7, CHRNA4, CHRNB3, CHRNA6, KCNH8, KCNJ6, GRIK1, HCN2). In our selection of these eight ion channels, rather than consider abundance in SNpc neurons alone, we assessed them across multiple criteria: (i) contribution to neural excitability, (ii) relative enrichment in the SN, (iii) low expression in non-brain tissues, (iv) expression in our ESC- and iPSC-derived neural cultures (**Supplementary Figure S3**), and (v) prior implication in PD. Our multi-parameter approach led us to select the eight channels shown in Figure 4. Heatmaps of z-score normalised gene expression showed these eight genes of interest have high expression in the SN relative to other brain regions (**Figure 4C**) and other tissues in the body, consistent with our objective to identify channels that may minimise potential off-target effects and broad neural silencing (**Figure 4D**). Furthermore, these ion channels were highly expressed in a subpopulation of dopaminergic neurons vulnerable to PD degeneration, marked by the expression of *SOX6* and *AGTR1*[53] (**Figure 4E**). This provided further reason to target these channels in a PD model. An extensive literature search identified nine ion channel modulators targeting the channels of interest (**Table 1**). These were applied to midbrain neural cultures to examine their effects on neuronal firing activity (**Supplementary Figure S4**). The doses used for each ICM were selected based on published studies in cultured neurons and iPSC-derived neuronal systems, with the broad ICM cocktail intended to achieve near-complete activity suppression and the SN-ICM doses chosen as an initial literature-guided starting point for selective and more moderate modulation. As there are currently no ion channel modulators that exclusively target SNpc dopaminergic neurons, we formulated an initial prioritised combination of ICMs that would theoretically have a combined effect upon SNpc-dopaminergic neurons while minimising off-target effects on non-SNpc dopaminergic neurons. Four compounds were subsequently selected to create a pilot substantia nigra-targeted ion channel modulator cocktail (SN-ICM; **Table 1,** α-conotoxin PIA, α-conotoxin MII, ML297, Fisetin), based on their target channel expression (**Supplementary Figure S3**), and their individual effects on midbrain neural cultures activity measured with MEAs (**Supplementary Figure S4**). Both α-conotoxins inhibit nicotinic acetylcholine receptors to decrease excitability, and ML297 activates G protein-gated inwardly rectifying K+ (GIRK2/Kir3.2) channels to promote membrane hyperpolarisation. Lastly, while fisetin potentiates hyperpolarization-activated, cyclic nucleotide-sensitive 2 (HCN2) channels, we observed that it consistently reduced neuronal firing rates in our midbrain cultures (**Supplementary Figure S4**).

Substantia nigra-targeted ICMs reduce the electrical activity of human midbrain neurons and enhance ATP levels.

To determine the potential of the SN-ICM cocktail to modulate neuronal electrical activity and enhance energy reserves, we exposed human midbrain neural cultures to the SN-ICM cocktail for 12 or 24 hours, followed by a recovery to baseline activity (**Figure 5A and Supplementary Figure S5**). In the preceding experiments, the generic ICM cocktail completely blocked neuronal electrical activity in all neurons, serving as a proof-of-concept to establish that reducing activity-dependent energy expenditure can improve neuronal energetics. Here, we aimed not for a full silencing of neuronal electrical activity, but instead a partial reduction in activity that may more closely reflect what a clinical ICM treatment would aim to achieve, as a total shutdown of dopaminergic neuron activity in the human brain may not be well tolerated or feasible. The SN-ICM cocktail reversibly decreased neuronal firing rates by ~50% and the number of active neurons ~30%, and reduced firing synchrony by ~50% (**Figures 5B-C**). While the SN-ICM cocktail

was designed to target ion channels enriched in SN dopaminergic neurons, future work will be required to further confirm the cellular specificity of its effects. Nevertheless, in human midbrain neural cultures, the SN-ICM-induced decrease in electrical activity led to a significant increase in intracellular ATP levels under basal conditions (**Figure 5D**). Furthermore, when we exposed midbrain neural cultures to a rotenone concentration that reduced intracellular ATP by ~40%, co-exposure to SN-ICM rescued intracellular ATP levels (**Figure 5E-F**). These findings demonstrate that SN-ICM cocktails can transiently reduce electrical activity in human midbrain neurons and increase neural ATP reserve, compensating for rotenone-induced ATP depletion.

Generic ion channel modulators are protective against ROS-mediated neurotoxicity.

We investigated whether raising neuronal ATP levels confers neuroprotection against oxidative insults, as dopaminergic neurons are particularly vulnerable to oxidative stress in PD[16,54,55]. Here, we exposed human midbrain neural cultures derived from ESCs (H9) or healthy iPSCs (**Supplementary Figure S6D,E**) to ICMs and/or H_2O_2 for 24 hours (**Figure 6, Supplementary Figure S6**). Inhibition of electrical activity was not neurotoxic (**Supplementary Figure S6A,E**) and produced a modest but reproducible neuroprotective effect on live cells and dopaminergic neurons exposed to reactive oxygen species (H_2O_2) (**Figure 6B-C and Supplementary Figure S6B,E,I**). Measurements of LDH, a metabolism-linked readout, might be confounded by altering neural energetics with rotenone and ICMs – consequently, we confirmed our observations with imaging-based cell viability counts (**Figure 6B**). This result showing neuroprotective benefits of ICMs was reproduced first in midbrain neural cultures derived from iPSCs, pooling six clones from three healthy individuals (two clones per individual) to harness potential individual variability (**Supplementary Figure S6D-G**), and again in commercial iCellDopa neural cultures (**Supplementary Figure S6H-J**).

Generic ion channel modulators are protective against rotenone-mediated lysosomal dysfunction.

The lysosomal system is important for the degradation of oxidatively damaged cellular components[56], and impairments to waste clearance have been implicated in PD. Lysosomes have highly acidic lumens required for efficient enzyme activity and are maintained by the action of ATP-dependent ATPase proton pumps. We used flow cytometry to examine whether ICM treatment could improve lysosomal function by increasing ATP availability, or even rescue it in the presence of mitochondrial dysfunction (**Figure 6D**).

Under basal (unstressed conditions), we observed an increase in lysosomal acidity and protease activity following broad ICM treatments **(Figures 6E, F)**. Furthermore, lysosomal acidity and protease activity was significantly reduced by rotenone and rescued by **ICM (Figures 6G-H)**. Such ICM-mediated rescue of lysosomal dysfunction was also validated using oligomycin, an alternative mitochondrial toxin that inhibits ATP synthase rather than complex I (**Supplementary Figures S7E-H**). Lysotracker Red and Magic Red fluorescent signals measured with FACS, used here to quantify lysosomal acidity and protease activity in neural cultures, can be altered by changes in the quantity and/or size of lysosomes. Therefore, we also used LAMP1 immunocytochemistry and confocal imaging to examine lysosome compartments in neurons and confirmed that neither rotenone nor the ICM cocktail induced significant perturbations in lysosome size or number (**Supplementary Figure S7C-D**). However, despite the clear effect of the generic ICM cocktail on lysosomal function, these results were not observed with optogenetic inhibition or SN-ICM **(Supplementary Figures S7A, B)**. This may reflect the differences in the magnitude of the ATP increase with SN-ICM and optogenetic inhibition, or technical limitations in the sensitivity of flow-cytometry-based measurements.

Overall, we find that metabolic impairments in human neural cultures in vitro (induced by rotenone or oligomycin) decrease neuronal lysosomal acidity and protease activity without altering lysosome number or size, and that such lysosomal dysfunction can be partially rescued by generic ICM treatments (**Figures 6G-H, Supplementary Figures S7C-H**).

PARK2 mutations impair dopaminergic neurons and exacerbate vulnerability to oxidative stress in human midbrain cultures.

We have demonstrated that ICM treatment can protect neurons against rotenone-induced energetic stress. However, while environmental exposure to rotenone and similar toxins has been reported to contribute to PD incidence[57], there is also a strong genetic component predisposing to PD[11,58]. The *PARK2* gene harbours some of the most common and highly penetrant mutations associated with early-onset PD[11]. *PARK2* mutations associated with PD [59] impair mitochondrial function and increase neuronal susceptibility to oxidative stress[50,60,61]. Therefore, next, we investigated the effects of ICMs in the context of *PARK2* mutations.

First, we generated healthy donor and *PARK2*-patient derived neural cultures. For this, we generated midbrain neural cultures using four clones from two PD patients carrying *PARK2* mutations (a *PARK2* heterozygous deletion in exons 3-5 and a *PARK2*-ex2del/c.202-203delAG mutation), pooling clones to capture a representative range of potential technical variance (**Figure 7A, Supplementary Figure S8**). Similarly, six clones from three healthy donors were generated and pooled to capture biological heterogeneity (**Figure 7A, Supplementary Figure S8**). These cultures consisted of LMX1A-, FOXA2-, and TH-expressing cells (**Figure 7C**), confirming the substantia nigra patterning and dopaminergic identity of the neural models. Furthermore, both the healthy and the *PARK2*-del cultures developed functional electrical activity (**Figure 7D**). Interestingly, *PARK2*-del cultures had a lower TH+ yield compared to the healthy donor cultures (**Figure 7C**).

Next, to further account for donor-specific genetic variability, we utilised an isogenic KOLF2.1J[62] pair consisting of a *PARK2* R275W SNV/SNV mutant and its isogenic control. For each line, we performed two independent neural inductions to assess the reproducibility of the observed phenotypes. We confirmed the presence of dopaminergic (TH+) neural populations and the development of electrical activity (**Figure 7E-G)**, and showed that *PARK2 R275W* cultures had lower TH+ yield, consistent with lower dopamine levels in supernatant compared to the isogenic control (**Figure 7H-I**).

We then aimed to establish a model of stress-induced cell death to be used for investigating the neuroprotective capabilities of ICM treatment. We exposed the cultures to a graded oxidative stress paradigm, ranging from antioxidant deprivation (mild stress) to the addition of H_2O_2 in the absence of antioxidants (strong stress). We demonstrated that *PARK2*-mutant neural cultures exhibited heightened vulnerability to both oxidative insults compared to healthy controls (**Figure 7J**), and TH+ neurons were more susceptible than non-TH neurons (**Figure 7K-L**).

Lowering neuronal electrical activity confers neuroprotection to PARK2-mutant neural cultures.

Next, we tested whether lowering neuronal electrical activity could protect *PARK2*-mutant neural cultures from H_2O_2-induced cell death. The neural cultures tested here comprised the two patient-derived lines harbouring distinct *PARK2* exon deletions and the CRISPR-engineered line carrying the homozygous *PARK2* R275W mutation (**Figure 8A**). These cultures were exposed to ICMs or SN-ICMs in combination with H_2O_2 or 6-OHDA for 24 hours to assess neurodegeneration as per the previously described experimental paradigm (**Figure 6**). Cultures co-exposed to ICMs and H_2O_2 showed less neurodegeneration, measured by both cell death and MAP2+ neurite degradation, than cultures exposed to H_2O_2 alone (**Figure 8B**). ICM treatment also partially protected TH+ neurons against H_2O_2-induced cell death (**Figure 8C**). Further, ICM co-exposure demonstrated neuroprotective trends across both patient lines individually, despite unequal patient representation in the pooled *PARK2*-del cultures (**Supplementary Figure S9**). Additionally, in both isogenic control and *PARK2* R275W cultures, TH+ neurons showed greater susceptibility than non-TH neurons yet ICM treatment protected both TH and non-TH subtypes (**Supplementary Figure S10A-C**).

H_2O_2 is a potent oxidative stressor, but it is non-selective in terms of which neurons it affects. Dopaminergic neurons appear more strongly affected by the *PARK2* mutations in vitro and more susceptible to oxidative stress and degeneration (**Figure 7J-L**). To investigate further the potential protective effect of ICMs on dopamine cells, we exposed the neural cultures to 6-hydroxydopamine (6-OHDA), a neurotoxin that selectively targets dopaminergic neurons. ICM treatment provided significant protection against 6-OHDA-mediated TH+ neurodegeneration (**Figure 8D, Supplementary Figure S10D-E**). Both ICM and SN-ICM treatments showed a non-significant trend toward increased dopamine concentrations in supernatant of cultures co-exposed to 6-OHDA, suggesting partial protection of functional dopamine release capacity (**Figure 8E, J**).

Like generic ICM, SN-ICM treatment also demonstrated significant neuroprotection against oxidative stress. Neural cultures co-exposed to H_2O_2 and SN-ICMs had more live cells and TH+ neurons, and increased MAP2+ neurite area than those exposed to H_2O_2 only (**Figure 8G,H, Supplementary Figure S10**). SN-ICMs also significantly reduced overall 6-OHDA-induced LDH cytotoxicity **(Figure 8G, I),** but SN-ICM only partially tended to protect TH+ neurons from cell death induced specifically by 6-OHDA without reaching significance in our experiments (**Figure 8I**), despite clear protective properties in the other assays. Overall, generic ICM significantly protected TH+ neurons against 6-OHDA-mediated cell death, and both generic ICM and SN-ICM treatments provided significant protection against oxidative stress-mediated TH+ neurodegeneration. These results suggest that lowering neuronal electrical activity with ICMs may provide neurons with some capacity to resist cellular stress that would otherwise lead to degeneration, in particular when susceptibility is increased by PD-linked mutations.

DISCUSSION

Despite the rising interest in neuronal metabolism in ageing and brain disorders, there are currently no therapeutic interventions that unequivocally enhance neuronal energetics. Various methods are under investigation towards this goal, including mitochondrial function enhancers, supplements targeting energetic pathways, and dietary interventions[1,63]. Recent studies suggest that boosting neuronal ATP via upregulating PGK1 can protect striatal dopaminergic neurons, which may reduce the risk of developing PD [2,22]. Although very promising, none of these approaches aims to modulate electrical activity, which is a primary source of ATP consumption in neurons[27]. Here, we propose an alternative, complementary strategy; we demonstrate the potential of ICMs or optogenetics to relieve neuronal energetic stress by transiently down-regulating electrical and synaptic activity. We show that providing short resting periods in neurons can enhance mitochondrial function, increase ATP levels and reprioritise scarce energetic reserves towards cellular mechanisms, such as lysosomal function or protection against oxidative insults, ultimately improving neuronal health. This approach was particularly effective in the context of mitochondrial impairments, which we mimicked pharmacologically with a complex I inhibitor, rotenone. Furthermore, it was also effective for protecting dopaminergic neurons against oxidative insults across three independent human iPSC models: two patient-derived lines harbouring distinct *PARK2* loss-of-function mutations (a homozygous deletion and a compound heterozygous variant), and a CRISPR-engineered isogenic *PARK2* homozygous single-nucleotide variant. We also identified a subset of ion channel targets specifically enriched in SNpc neurons, which are particularly vulnerable in Parkinson's disease. We showed that the SN-ICM cocktail can transiently reduce electrical activity and increase neuronal ATP levels. While these results remain preclinical and exploratory, they support further investigation of ion channel modulation as a potential neuroprotective approach in PD and related neurodegenerative disorders.

Several studies indicate that PD and other brain disorders often begin with the degeneration of synapses and neural projections[17,18,64,65]. Neurites require large amounts of ATP for ATPase pumps to generate and propagate action potentials over long distances effectively. Similarly, synaptic sites require high ATP levels to convert electrical inputs to neurotransmitter release and maintain critical neurotransmission[28,66]. Indeed, synaptic vesicle cycling and restoration of post-synaptic ion gradients are major drivers of activity-dependent metabolic demand [28,67]. Because these processes are concentrated at highly active synaptic,

axonal and dendritic compartments, they may be especially vulnerable to proteostatic, oxidative and metabolic stress[29,50,68]. By modulating ion channels enriched in these compartments, ICMs may reduce the broader cascade of activity-dependent energy consumption. In principle, overactive synapses may experience the greatest local energetic benefit from activity reduction, potentially enabling ATP redistribution to vulnerable neuronal compartments. Similarly, overactive neurons may derive the greatest metabolic benefit from transient reductions in electrical load to support rest and repair [34,69,70]. To understand which cellular compartments will benefit most from increased ATP availability, future studies interrogating how ATP is distributed across the cell during ICM treatment will be important.

We showed that lowering neuronal electrical activity increases the resilience of neurons against oxidative insults. This may be associated with reduced mitochondrial oxidative phosphorylation (OxPhos) and glycolysis demand; reduced OxPhos decreases endogenous oxidative stress, while lower glycolysis may redirect glucose into the antioxidant-generating pentose phosphate pathway[71], enhancing neuronal capacity to combat oxidative damage. In addition, increasing ATP availability may enhance neuronal health and resilience through energy-consuming processes such as DNA repair, protein synthesis[72], and autophagy. For example, the autophagy-lysosomal pathway, essential for degrading damaged cellular components, relies on ATP for lysosomal acidification and enzyme activity[73]. Our findings indicate that ICM treatment raises lysosomal acidity and cathepsin activity, which could help maintain mitochondrial quality and suppress the spread of aggregated proteins like α-synuclein and tau[19,48,74]. Enhancing autophagy has been proposed as a therapeutic strategy for clearing toxic protein aggregates in PD[75]. However, it is highly ATP-dependent and vulnerable to energetic stress[76]. Consequently, attempts to upregulate the autophagy-lysosomal pathway may further increase cellular energy requirements and overwhelm an already stressed system in aged or PD-affected brains. Restoring ATP levels through ICMs could thus bolster autophagy function, aiding in the clearance of pathogenic proteins. This strategy may also be applicable to other neurodegenerative diseases characterised by reduced lysosomal acidification, such as Alzheimer's disease and frontotemporal dementia[77,78].

PARK2 mutations account for ~0.3% of global PD cases[11] and are well-established drivers of mitophagy impairments and cellular vulnerability. Impaired mitochondrial function can lead to reduced cellular energetics and heightened sensitivity to oxidative stress, as we observed in *PARK2*-mutant iPSC-derived neurons. Familial PD represents ~15% of all cases and is frequently associated with disruptions in these same pathways. For example, mutations in other PD-associated genes such as *PINK1*, *DJ-1*, and *LRRK2* all impair mitochondrial function and exacerbate susceptibility to oxidative stress [11,79-81]. Therefore, the neuroprotection observed in *PARK2*-mutant neurons following ICM treatment may extend beyond *PARK2*, raising the possibility of broader translational relevance across multiple genetic backgrounds. Future validation in additional PD and neurodegenerative models will be essential to confirm this potential. In addition, deeper analyses will be important to determine whether ICM treatment alleviates *PARK2*-associated mitochondrial abnormalities, and whether reducing activity-dependent ATP demand directly improves mitochondrial health.

Our results also provide novel evidence that targeted modulation of specific ion channels, like GIRK2 and nicotinic acetylcholine receptors (nAChRs), effectively lowers neuronal electrical activity while raising neuronal energy levels. Despite having a more modest effect on energy levels than the broad ICM cocktail (TTX), the SN-ICM cocktail still conferred protection to TH+ dopaminergic neurons against oxidative stress, demonstrating that even a partial, non-silencing reduction in activity can provide bioenergetic and neuroprotective benefits. The compounds in the SN-ICM cocktail were specifically chosen for their activity on ion channels enriched in the SNpc, but they only represent a proof-of-concept pharmacological tool, rather than a final, optimised therapeutic cocktail that acts exclusively on SNpc dopaminergic neurons. Potential off-target effects could be reduced further with ICMs more specific to the ion channel subunits enriched in SNpc. For example, peptides extracted from animal venoms[82,83], such as conotoxins, which show high selectivity for dopaminergic neuron-specific ion channels like α6* nAChRs[84,85] could enhance

ICM efficacy and reduce the likelihood of modulating brain regions outside the SNpc. Similarly, enhanced selectivity for GIRK2 homotetramers could be developed by modifying compounds like VU0529331[86]. Clinical translation of potential ICM therapies will require further preclinical research, including fine-tuning ICMs to reach stringent pharmacological specificity and *in vivo* toxicity screening. Future studies must also establish whether the metabolic benefits of transiently reducing neuronal electrical activity can be achieved within a safe pharmacological window for dopaminergic signalling and patient tolerability.

Safinamide, a potent monoamine oxidase B inhibitor that increases dopamine bioavailability, has shown effectiveness in treating PD[87-89]. Interestingly, Safinamide also inhibits voltage-gated sodium channels (Na_v) and modulates calcium channels, which reduces excessive glutamatergic input to the striatum[90]. This Na_v inhibitory effect is not specific to the SNpc or striatum and may also affect cortical excitatory neurons that project to the striatum[89,90]. Nevertheless, Safinamide is safe and well-tolerated, with low rates of serious adverse events reported[87]. Although the extent of Na_v channel inhibition at clinical doses of Safinamide is not fully understood, its tolerability suggests that some degree of ion-channel modulation can be compatible with clinical use, although this cannot be assumed for the SN-ICM compounds tested here. Furthermore, the Safinamide off-target effect on ion channels may have therapeutic benefits in unexpected ways by improving neuronal metabolic homeostasis.

Our study demonstrates that neuronal energetic homeostasis can be modulated using pharmacological and optogenetic strategies to reduce neuronal electrical activity. This has potential future translational applications, as some small-molecule ICMs can be administered systemically and cross the blood-brain barrier. Nearly 20% of current small-molecule therapeutics target ion channels, making them the third most common drug target after kinases and G-protein-coupled receptors[91]. ICMs offer specificity, potency, stability, speed, and reversibility in modulating their molecular targets, making them promising candidates for therapeutic development. Other approaches for modulating neuronal electrical activity not tested here could also be explored to regulate neuronal energetics. For instance, deep brain stimulation (DBS) is widely used to modulate neuronal activity in specific brain regions, particularly in treating PD cases less responsive to dopaminergic therapies. DBS primarily alleviates motor symptoms by modulating activity within basal ganglia circuits, commonly targeting the subthalamic nucleus or globus pallidus internus[92]. While current DBS treatments do not directly target dopaminergic neurons in the SNpc, DBS could be repurposed to transiently inhibit the SNpc neurons.

Transiently inhibiting SNpc activity may initially seem counterintuitive, as reduced dopaminergic signalling may worsen PD symptoms during the treatment window. However, this could represent a temporary trade-off if it yields longer-term bioenergetic and neuroprotective benefits – a highly sought-after goal in treating PD and other neurodegenerative diseases that has been difficult to achieve. Any such approach would need to be carefully optimised and evaluated in combination with symptomatic dopamine replacement therapies. Repeated short-term interventions (e.g., daily or weekly, lasting hours) that transiently reduce neuronal electrical activity could provide vulnerable neurons with periodic metabolic relief, allowing them to conserve energy and engage repair processes without requiring sustained inhibition of dopaminergic signalling. Alternatively, a chronic but more modest reduction in neuronal electrical activity may provide bioenergetic relief while minimising disruption to dopaminergic signalling. Our work suggests that targeted modulation of neuronal electrical activity may be a strategy worth further preclinical investigation to slow neurodegenerative processes in PD and related disorders.

CONCLUSION

Neurons that are metabolically impaired, or forced to maintain circuit function while compensating for chronic cell loss, pose a major therapeutic challenge in neurodegenerative disease. Their synapses, dendrites and axons are among the most energy-demanding compartments, making them especially susceptible to metabolic stress. These sites are also densely populated with ion channels, presenting promising targets for ICMs. Our study demonstrates that down-modulating neuronal electrical activity can effectively increase

neuronal energy levels, offering neuroprotection against oxidative stress and enhancing some aspects of lysosomal function. We propose that transiently reducing neuronal electrical activity may provide neurons with a "rest" period, allowing them to replenish ATP reserves, repair damage, or clear cellular waste and potentially interrupt the cycle of neurodegeneration. PD, which is characterised by the localised degeneration of a subtype of dopaminergic neurons in the SNpc with high electrical activity and metabolic requirements, may be particularly amenable to this approach.

This study offers a foundation for future development and preclinical testing of more selective neuron-type-specific ICMs, and for evaluating whether transient reductions in neuronal electrical load can be achieved safely *in vivo*. Overall, the current findings support further investigation of electrical activity modulation as a strategy to alleviate neuronal energetic stress, which may have future therapeutic potential for PD and other neurodegenerative disorders.

Author Contributions

C.B. and R.A. conceived and designed the study and experiments with input from T.S.; B.M., P.M., and R.A. performed experiments; B.M., P.M., R.A., A.A.A., and I.I analysed the data and prepared the figures; B.M. generated, characterized and cultured the neural lines; P.M. performed and analysed the whole-cell patch clamping experiments; B.M., P.M., I.I, and R.A. performed the immunohistochemistry and confocal imaging; B.M. performed the live-cell imaging; B.M. established the optogenetic protocols; B.M., P.M., A.A.A., and I.I performed the multielectrode array experiments and analyses; R.A. performed and analysed the metabolic experiments; R.A. performed and analysed the lysosome experiments; P.M. conducted the transcriptomics analysis. R.A., B.M., P.M., and C.B. wrote the manuscript with inputs from all authors.

Acknowledgements

We thank Andy Robert (Flinders University) and Alejandra Noreña Puerta (SAHMRI) for LAVA board production and testing, and Nicole Repina, Thomas McClave and David Schaffer for kind and generous guidance regarding the LAVA board design. Flow cytometry analysis and cell sorting was performed at the Adelaide Health and BioMedical Precinct Cytometry Facility (SAHMRI). The Facility is generously supported by the Detmold Group, McMahon Family, Australian Cancer Research Foundation, Cancer Council and Australian Government through the Zero Childhood Cancer Program. We acknowledge the contribution of the South Australian Genomics Centre (SAGC) in the generation of data used in this publication. The SAGC is supported by its founding partner institutes and by BioPlatforms Australia as part of the Australian Government's National Collaborative Research Infrastructure Strategy (NCRIS). We also acknowledge the Women's and Children's Hospital for karyotyping cell lines.

Funding sources.

This project was funded by the Michael J Fox Foundation, The Hospital Research Foundation and the Shake it Up Foundation; CB is the recipient of an Australian Research Council Future Fellowship (FT230100138) funded by the Australian Government. PM and RA are supported by Flinders University and Australian Government Research Training Program scholarships; Further support was obtained from Angelique and Michael Boileau, and the Rebecca L. Cooper Foundation (CB).

Declaration of Interests

The authors declare no competing interests.

DATA AND CODE AVAILABILITY

All original code has been deposited at GitHub and is publicly available as of the date of publication.

Datasets presented in **Supplementary Figure S3** were pre-processed according to previous methods[49] [https://github.com/bardylab/RNAseq_iPSC_PD].

Post-mortem single nuclei RNA-sequencing data was accessed via the Single Cell Broad Institute (https://singlecell.broadinstitute.org/single_cell/study/SCP1768/).
Genotype-Tissue Expression (GTEx)[127,128] v8 transcriptome data (dbGaP Accession phs000424.v8.p2, accessed January 2023) and sample annotation information for 55 adult tissue types were retrieved from the GTEx portal (http://www.gtexportal.org/).

Any additional information required to reanalyse the data reported in this paper is available from the lead contact, Prof. Cedric Bardy (cedric.bardy@sahmri.com), upon reasonable request.

METHODS

Human iPSCs

Human fibroblasts were obtained from skin biopsies of three healthy individuals and two diagnosed PD patients carrying *PARK2* mutations: one *PARK2* heterozygous deletion of exons 3-5 and one *PARK2*-ex2del/c.202_203delAG mutation. All individuals were male, with a mean age of 55 years in both the healthy control and PD groups. All iPSC lines were confirmed to express pluripotency markers and to have normal karyotypes.
The KOLF2.1J isogenic control line (JIPSC001000, derived from HPSI0114i-kolf_2; barcode 3540932782) and the PARK2 R275W SNV/SNV line (JIPSC001412, derived from JIPSC001000; barcode 3541049549) were obtained from The Jackson Laboratory. Authentication and quality control were performed by the supplier and confirmed in-house, as described previously[62].

Karyotyping

Neural progenitors were cultured in T25 flasks and transferred to the Women's and Children's Hospital, SA Pathology, Cytogenetics, Genetics and Molecular Pathology, for G-band karyotyping. Briefly, cells at 70–80% confluency were treated with colchicine (0.1 mg/L) for 2–3 h to arrest cells in metaphase. Cells were then washed, dissociated and pelleted. Cell pellets were incubated with 8 mL hypotonic solution (0.075 M KCl/0.8% trisodium citrate) for 25 min, then fixed with Carnoy's fixative (3:1 methanol/acetic acid). Fixed cells were spread onto slides and analysed. A minimum of 20 metaphases were analysed for each cell line.

Differentiation into neural cultures

All neuronal generation, culture and sorting procedures were conducted according to previously established protocols[45,46]. Briefly, iPSCs and human female embryonic stem cells (hESCs; WiCell, WAe009-A; RRID:CVCL_9773) were maintained in mTeSR1 medium (STEMCELL Technologies) on tissue cultureware coated with hESC-qualified Matrigel (Corning), according to the manufacturer's instructions.
Neural progenitor cells (NPCs) were generated using an embryoid body (EB)-based protocol with dual SMAD inhibition, as described previously[93], and were maintained in midbrain or cortical neural progenitor medium. Midbrain neural progenitor medium consisted of DMEM/F12 + GlutaMAX supplemented with 1× SM1, 1× N2-A, 200 ng/mL sonic hedgehog (SHH; PeproTech), 100 ng/mL FGF8b (PeproTech), 200 nM ascorbic acid (Sigma) and 1 µg/mL laminin. Cortical neural progenitor medium consisted of DMEM/F12 + GlutaMAX supplemented with 1× SM1 with vitamin A, N2-A , 10 ng/ml FGF2, 200 nM ascorbic acid, and 1 µg/ml laminin. Medium changes were performed every other day, and NPCs were expanded for six passages before differentiation.

For neuronal differentiation and maturation, NPCs were dissociated and plated at 2×10^5 cells/cm² onto tissue culture plates coated with 5 µg/mL laminin (Thermo Fisher Scientific) in midbrain neural maturation medium (NMM) or cortical neural maturation medium (coNMM). NMM consisted of BrainPhys Neuronal Medium supplemented with factors to promote midbrain fate: N2-A, SM1, 200 nM ascorbic acid, 1 µg/mL laminin, 20 ng BDNF (STEMCELL Technologies), 20 ng GDNF (STEMCELL Technologies) and 0.5 mM dibutyryl cyclic AMP (Sigma-Aldrich). coNMM consisted of BrainPhys neuronal medium supplemented with N2 Supplement A (STEMCELL Technologies), SM1 without vitamin A (STEMCELL Technologies), 200 nM ascorbic acid, 1.2 nM laminin (1 µg/ml; Gibco), 20 ng of BDNF (STEMCELL Technologies), 20 ng of GDNF (STEMCELL Technologies), 10ng/mL IGF (STEMCELL Technologies), and 0.5 mM dibutyryl cyclic adenosine 50 -monophosphate. Neurons were maintained for 14 days after differentiation, with half-medium changes every 2–3 days, before being replated onto tissue culture plates coated with 10 µg/mL poly-L-ornithine (Sigma-Aldrich) and 5 µg/mL laminin in NMM containing half concentrations of growth factors. If cell lines were to be pooled for experiments, they were pooled during the replating step. Cultures were maintained at 37 °C and 5% CO_2 in standard tissue culture incubators.
For multielectrode array (MEA) recordings, neural cultures were replated at 300,000 viable neurons in a 10 µL droplet of cell suspension seeded directly over the recording electrodes of each MEA well. The final well volume was 400 µL. For maintenance of all cultures, medium was exchanged on Mondays, Wednesdays and Fridays by replacing half of the culture medium with fresh NMM, using either a JANUS Liquid Handler Workstation (PerkinElmer) or Assist Plus (Integra).
Cultures were matured for at least 35 days for experiments.

Commercial dopaminergic neural cultures
iCell DopaNeurons (FUJIFILM Cellular Dynamics) were purchased as cryopreserved, terminally differentiated human dopaminergic neurons. Cells were thawed according to the manufacturer's protocol and cultured in BrainPhys neural maturation medium.

Multielectrode array recordings
MEA recordings were acquired using a Maestro Pro MEA system (Axion Biosystems). Cell cultures in Lumos 48-well MEA plates (M768-tMEA-48OPT, Axion Biosystems) were maintained at 37 °C and 5% CO_2 during recordings. Recordings were started 10 min after transferring plates into the MEA system. AxIS Navigator acquisition software (Axion Biosystems) was used to sample voltage potentials simultaneously across 16 electrodes per well. The sampling frequency was 12.5 kHz, and a Butterworth band-pass filter of 200–3000 Hz was applied.
The spike-detection threshold was set on a per-electrode basis and defined as voltage deflections exceeding 6 standard deviations from the mean background noise. Raw recordings were converted to .spk files in AxIS, and .spk files were converted to .nex files using the Axion Data Export Tool. Single-cell spike sorting of .nex files was performed in Plexon Offline Sorter version 4.5 (Plexon Inc.) using a 3D T-Dist E-M algorithm with a D.O.F. multiplier of 10 and an initial number of units of 8. Short inter-spike interval (ISI) waveforms were excluded during spike sorting. Single-cell spike-sorted files (.nex and .mat) were processed using Neural Metric Tool version 3.1.7 to generate .csv metric files.
Network events were defined by ISI thresholding and required a minimum of 50 spikes, a maximum ISI of 80 ms, and participation of at least 35% of all neurons. Bursts were defined by ISI thresholding and required a minimum of 5 spikes with a maximum ISI of 100 ms. Further data processing was performed in Python 3 (Python Software Foundation) using custom scripts for data collation and for generating time-series plots, heatmaps and raster plots.

Lentiviral transduction
Lentiviral vectors were produced in Lenti-X 293T cells (Takara Bio) cultured in high-glucose DMEM without glutamine (Life Technologies), supplemented with 10% fetal bovine serum (Life Technologies), 4 mM GlutaMAX (Life Technologies) and 1 mM sodium pyruvate (Sigma). Cells were cultured on tissue cultureware coated with 0.002% poly-L-lysine (Sigma).

Lenti-X 293T cells were transfected with 12.2 µg lentiviral transfer plasmid, either LV-pLenti-hSyn-eNpHR3.0-EYFP or LV-pCSC-Synapsin(0.5kb)-MCS-EGFP, a derivative of pCSC-SP-PW-EGFP, together with packaging plasmids: 8.1 µg pMDL/RRE, 3.1 µg pRSV/REV and 4.1 µg pCMV-VSVg. Transfection was performed using polyethylenimine. Culture medium was exchanged 6 h after transfection. Supernatant containing lentiviral particles was collected 3 days after transfection, filtered through a 0.45 µm SFCA filter, and ultracentrifuged at 25,000 rpm (Beckman) for 2 h at 4 °C. Viral pellets were resuspended in HBSS, and viral titre was determined using the Lenti-X qRT-PCR Titration Kit (Clontech) according to the manufacturer's instructions. Neuronal cultures were transduced with titre-matched lentiviral vectors (2.67 × 10^3 viral RNA copies/cell) for 48 h before washout.

Optogenetic stimulation

Optical stimulation parameters were configured using Stimulation Studio software in AxIS Navigator. Optical stimulation was performed using either a Lumos optical stimulator (Axion Biosystems) or a custom-built LAVA board optical controller[94]. Schematics describing the stimulation protocols are shown in Figure 3. Halorhodopsin (eNpHR3.0) was stimulated using orange light at 594 nm and 15% intensity. Lumos orange LED stimulation at 100% intensity is >2.2 mW/mm² according to the manufacturer.

Whole-cell patch clamp recordings

Whole-cell patch clamp recordings were performed using previously established protocols[95]. Coated coverslips[46] containing midbrain neural cultures were transduced with a Synapsin:GFP lentiviral vector before transfer to a recording chamber perfused with artificial cerebrospinal fluid (ACSF) at room temperature (21–23 °C) using a Minipuls 3 pump (Gilson). Before perfusion, ACSF osmolality was measured using a Fiske Micro-Osmometer (model 210, Advanced Instruments) to confirm that it was within the required range of 300–310 mOsm. ACSF contained 121 mM NaCl, 4.2 mM KCl, 1 mM $MgSO_4$, 29 mM $NaHCO_3$, 0.45 mM NaH_2PO_4, 0.5 mM Na_2HPO_4, 1.1 mM $CaCl_2$ and 20 mM glucose, and was continuously bubbled with 95% O_2 and 5% CO_2.

Recordings were performed using an upright Olympus BX51 microscope equipped with a 40× water-immersion objective and a PCO.Panda 4.2 camera. A CoolLED pE-300 illumination unit at 460 nm was used to visualise Synapsin:GFP-expressing neurons. Borosilicate glass filaments (BF100-50-7.5, Sutter Instrument) were pulled to an open resistance of 3–6 MΩ using a P-1000 micropipette puller (Sutter Instruments). Patch pipettes were filled with an intracellular solution adjusted to physiologically similar pH and osmolality (pH 7.3, 290–300 mOsm). The intracellular solution contained 130 mM K-gluconate, 6 mM KCl, 4 mM NaCl, 10 mM Na-HEPES, 0.2 mM K-EGTA, 0.3 mM Na-GTP, 2 mM Mg-ATP, 0.2 mM cAMP, 10 mM D-glucose, 0.15% biocytin and 0.06% rhodamine.

Whole-cell recordings were amplified using a Digidata 1550B/Multiclamp 700B system, digitised and sampled using pClamp software (v10.7, Molecular Devices) at 50 kHz for voltage-clamp recordings and 100 kHz for current-clamp recordings. Before formation of a gigaohm seal, the pipette was offset so that the baseline was approximately 0 pA. To record voltage-gated sodium (Na^+) and potassium (K^+) currents, cells were held at −60 mV in voltage-clamp mode and injected with +5 mV steps across 20 sweeps after an initial step to −65 mV. Cells were held in C = 0 mode to record resting membrane potential.

Action potential firing and kinetics were recorded by applying sufficient current to hold neurons at −60 mV in current-clamp mode, followed by 500 ms depolarising current steps for 15–20 sweeps. If the holding current exceeded −100 pA, the recording was considered poor quality and aborted. AMPA-mediated events were recorded at −60 mV in voltage-clamp mode, whereas GABA-mediated events were recorded at 0 mV in voltage-clamp mode, corresponding to the reversal potentials for sodium and chloride, respectively. Events were recorded for 3 min in gap-free mode.

To exclude unhealthy neurons and suboptimal recording conditions, only neurons with a seal resistance >1 GΩ and access resistance <20 MΩ were included in the final analysis. If patch quality or cell health deteriorated such that quality-control checks were failed, the recording was aborted and only data acquired before quality deterioration were included.

Neurons were classified into action potential types 1–5 according to a previously reported framework[47] based on combined morphological, transcriptomic and electrophysiological features. Type 1 neurons express small sodium currents but cannot fire an action potential above −10 mV; these were considered aborted action potentials. Type 2 neurons fire only one action potential above −10 mV, followed by a plateau. Type 3 neurons fire one action potential above −10 mV, typically followed by one or more aborted action potentials. Type 4 neurons fire more than one action potential above −10 mV but do not fire at >10 Hz. Type 5 neurons fire action potentials at >10 Hz.
All whole-cell patch clamp data were analysed using custom-built Python scripts[95].

Immunocytochemistry and high-content imaging

Cells grown in 384-well CellCarrier Ultra imaging plates (PerkinElmer) were washed once with DPBS or BrainPhys Imaging medium and fixed in 4% paraformaldehyde (PFA) for 10 min at room temperature. Fixed cells were washed three times with DPBS and once with Tris-buffered saline (TBS), then permeabilised in TBS++ (TBS containing 0.2% Triton X-100 and 3% donkey serum) for 1 h at room temperature. Primary antibodies were diluted in TBS++ and incubated overnight at 4 °C. After three washes with TBS, cells were incubated for 30 min at room temperature in TBS++, then for 1 h at room temperature in TBS++ containing donkey secondary antibodies conjugated to fluorescent tags (1:250). Cells were then stained with DAPI and washed as described above.
All liquid transfers were performed using a JANUS liquid handler (PerkinElmer). Images were acquired using an Operetta CLS High-Content Imaging System (PerkinElmer) and Harmony 4.9 software (PerkinElmer). Multiple fields of view capturing >75% of each well and consisting of 10–20 z-stacks at 0.5–1 µm intervals were acquired for each well. Custom Harmony analysis pipelines were used to analyse maximum-projection images.
For lysosome staining, in-house sheep anti-LAMP1 antibody was used at 1:300 dilution and was obtained from the Lysosomal Health in Ageing, Hopwood Centre for Neurobiology group at SAHMRI[96,97]. Fluorescent secondary antibody staining was performed using donkey anti-sheep Alexa Fluor 488.
For neurotoxicity staining, cells were stained with DAPI, chicken anti-MAP2 (1:2000), mouse anti-TH (1:75 or 1:1000), and/or rabbit anti-NeuN (1:2000). Secondary antibody staining was performed with donkey anti-mouse Alexa Fluor 568 (1:250), donkey anti-chicken Alexa Fluor 488 (1:250), and donkey anti-rabbit Alexa Fluor 647 (1:250).

Live cell imaging

Live-cell imaging was performed using an IncuCyte system (Sartorius, version 2024A). 16 non-overlapping fields of view (FOV) per well were acquired using the Adherent Cell-by-Cell scan at 20X magnification every 24 hours between 60 and 80 days in vitro (DIV) in the green, orange, and phase channels. GFP- and tdTomato-positive areas were quantified using the Basic Analyzer analysis module, and confluence was calculated using adaptive segmentation and mean intensity filters as the percentage of total FOV area occupied by fluorescent signal.

ATP Assay

CellTiter Glo Luminescent Cell Viability (Promega) assays were performed according to the manufacturer's protocol to measure the ATP levels of cultures. Luminescence readings were taken in a GloMax Discover Microplate Reader (Promega). ATP standards at several concentrations were used as positive controls and to standardise sample readings.
Dopamine ELISA
Dopamine concentrations in conditioned media were quantified using a commercially available dopamine ELISA kit (Abcam, Cat. No. ab285238; Lot Nos. 1123071-1 and 1132562-1) according to the manufacturer’s instructions, with minor modifications. Conditioned media were collected from cultures maintained in BrainPhys basal medium, cleared by centrifugation to remove debris, and stored at −80 °C until analysis. To account for potential matrix effects, the standard curve was prepared in BrainPhys basal

medium rather than the supplied assay buffer. Absorbance was measured at 450 nm using a microplate reader, and dopamine concentrations were interpolated from the BrainPhys-based standard curve.

Culture Treatments

Rotenone was reconstituted in pure acetone at 100 mM and diluted in NMM to working concentrations immediately before treatment. Working concentrations used for treatments were the IC_{50} for each neural differentiation. Treatment durations are indicated in the figure legends and results. Full medium changes were performed to start treatment.

6-OHDA was reconstituted in sterile water. Stock solutions were diluted in culture medium to working concentrations of 75-140μM before treatment. Treatment concentrations and durations are indicated in figure legends. Full medium changes were performed to start treatment.

H_2O_2 was diluted in culture medium to working concentrations before treatment. Treatment concentrations and durations are indicated in figure legends. Full medium changes were performed to start treatment.

For the generic ICM cocktail, tetrodotoxin (TTX) was reconstituted in pH 4.8 PBS into 1 mM aliquots. NBQX and APV were each reconstituted in H_2O into 10 mM aliquots. TTX, NBQX and APV were diluted 1:1000 in NMM to final working concentrations of 1 μM, 10 μM and 10 μM, respectively. Full medium changes were performed to start and terminate treatment. Treatment durations are indicated in the figure legends.

For the SN-ICM cocktail, fisetin, ML297 and α-conotoxin PIA were reconstituted in DMSO into 10 mM stocks for fisetin and ML297, and 0.5 mM stock for α-conotoxin PIA. α-Conotoxin MII was reconstituted in sterile water into a 0.5 mM stock. Fisetin and ML297 were diluted 1:500 to 20 μM each, and both conotoxins were diluted 1:2500 to 200 nM each. Compounds were added to culture medium before addition to experimental plates. A half-medium change was then used to dilute the compounds to final concentrations of 10 μM for ML297 and fisetin, and 100 nM for both conotoxins. The cocktail was removed by full medium change, and cells were allowed to recover.

For other ICMs, VU0529331, UBP310 and UBP302 (Focus Bioscience) were reconstituted in DMSO and diluted in culture medium to final concentrations of 10 μM. Dihydro-β-erythroidine hydrobromide (Focus Bioscience) and Brilliant Blue G (Sigma-Aldrich) were reconstituted in sterile water and diluted in culture medium to final concentrations of 10 μM and 50 nM, respectively.

Flow cytometry

LysoTracker Red DND-99 was added to culture medium at a final concentration of 50 nM, and cultures were incubated for 1 h at 37 °C and 5% CO_2. Samples were stained with 5 μM DRAQ5 for 5 min at 37 °C, then dissociated using Accutase. Samples were transferred to tubes using ice-cold BrainPhys Imaging medium and centrifuged at 300 r.c.f. for 5 min at 4 °C. Supernatant was aspirated, and cell pellets were resuspended in ice-cold BrainPhys Imaging medium. Samples were filtered into flow tubes through 70 μm nylon mesh cell strainers and kept on ice. DAPI was added to each sample at a final concentration of 2 μM, 60 s before analysis using a BD LSRFortessa X-20 Cell Analyzer (BD Biosciences).

LysoTracker Red was excited using a 561 nm yellow-green laser, and emission was detected with a 610/20 nm band-pass filter. DRAQ5 was excited using a 640 nm red laser, and emission was detected using a 780/60 nm band-pass filter. DAPI was excited using a 405 nm violet laser and detected with a 450/50 nm band-pass filter. For lysosomal cathepsin activity, Magic Red Cathepsin L was added to culture medium at a final concentration of 50 nM instead of LysoTracker Red. Magic Red was excited using a 561 nm yellow-green laser, and emission was detected with a 610/20 nm band-pass filter. Data were analysed using FlowJo software. The proportion of viable cells, defined as DAPI-negative cells, was read directly from FlowJo analysis.

Gates were first applied to select DRAQ5-positive events and were compared against time to identify and exclude aberrant time points during recordings. Following DRAQ5 selection, single-cell events were gated using forward scatter area (FSC-A) versus forward scatter height (FSC-H). Single-cell events aligned approximately along the diagonal between the lower left and upper right corners; events substantially outside this diagonal were considered doublets or higher-order multiples. Small debris was excluded using

side scatter area (SSC-A) versus FSC-A. Viable cells were gated as DAPI-negative events. Using this gated viable population, mean fluorescence intensity of LysoTracker Red or Magic Red was calculated. Flow cytometry was performed at the ACRF Cellular Imaging and Cytometry Core Facility at SAHMRI.

Seahorse extracellular flux assays

Culture metabolism was measured using an Agilent Seahorse XFp Analyzer with Mito Stress Test and Real-Time ATP Rate Assay kits (Agilent). Assays were performed according to the manufacturer's instructions. Oxygen consumption rate (OCR) and extracellular acidification rate (ECAR) were measured at baseline and after acute sequential injection of oligomycin, FCCP, rotenone and antimycin A according to kit instructions.

Neural cultures were reseeded at 3×10^4 cells/well at days 28–35 of maturation into Seahorse XFp miniplates (Agilent), then matured for a further 7 days before assays. Mito Stress Test assays were performed in NMM, whereas Real-Time ATP Rate Assays were performed in XF-ACSF, an ACSF formulation modified for assay compatibility: 150 mM NaCl, 4.2 mM KCl, 1.1 mM $CaCl_2$, 1 mM $MgSO_4$, 10 mM HEPES, 0.45 mM NaH_2PO_4, 0.5 mM Na_2HPO_4 and 10 mM glucose, adjusted to pH 7.4. The buffer factor for XF-ACSF was determined according to the Agilent Seahorse XF Buffer Factor protocol.

For the Mito Stress Test, final injected drug concentrations were 1.5 µM oligomycin, 30–100 µM FCCP, determined according to an FCCP titration curve as per the manufacturer's instructions, 1 µM rotenone and 1 µM antimycin A. For the Real-Time ATP Rate Assay, final injected drug concentrations were 1.5 µM oligomycin, 1 µM rotenone and 1 µM antimycin A. Output files were processed using the Agilent Seahorse Analytics online tool. Wells were either fixed in 4% PFA and stained with DAPI immediately after each assay, or stained with Hoechst and imaged live after treatment but immediately before starting the Seahorse assay. Well data were normalised to total DAPI or Hoechst area within the sensor area of Seahorse plate wells, measured in ImageJ.

RNAseq sample preparation for in-house bulk-PSC dataset

mRNA was isolated in triplicate for PSC-derived midbrain neural cultures and prepared for sequencing according to previous methods[49]. RNA samples were assessed for quality (2100 Bioanalyzer, Agilent) and quantity (Qubit fluorometer, Thermo Fisher Scientific), and up to 1 µg of total RNA per sample was processed for cDNA synthesis, amplification and library construction using the TruSeq Stranded mRNA library preparation kit (Illumina). Constructed libraries were purified using Agencourt AMPure XP beads (Beckman Coulter #A63881), quantified for yield (Qubit fluorometer), and quality-assessed by fragment analysis (2100 Bioanalyzer). Sample libraries were then multiplexed and sequenced on a NextSeq 500 sequencer (Illumina) using 75-bp single-end SBS chemistry.

GTEx RNA-sequencing data processing.

Genotype-Tissue Expression (GTEx)[127,128] v8 transcriptome data (dbGaP Accession phs000424.v8.p2, accessed January 2023) and sample annotation information for 55 adult tissue types were retrieved from the GTEx portal (http://www.gtexportal.org/). The read counts were read into R using the read.gct function from the CePa (Centrality-Based Pathway Enrichment) package (v0.7.0). Transcriptome samples were filtered to only include those with an RNA integrity (RIN) score of 7.5 or higher (SMRIN column of annotation file) and that have been identified by the GTEx Consortium to be best suited for RNA-seq analysis (SMAFRZE column of annotation file). Using the SMTS column of the annotation file, data was subset for brain tissue, then was further subset using the SMTSD column of the annotation to separate the substantia nigra (SN, n = 19) samples from other brain region samples (consisted of amygdala (n= 14), anterior cingulate cortex (ACC, n = 27), caudate nucleus (BG_NC, n = 126), cerebellar hemisphere (CH, n = 111), cerebellum (n = 10), cortex (n = 5), frontal cortex BA9 region (FC_BA9, n = 73), hippocampus (n = 38), hypothalamus (n = 51), nucleus accumbens (BG_NA, n = 82), putamen (BG_Putamen, n = 70) and spinal cord cervical (SCC, n = 56). For substantia nigra vs other tissues in the body, data was QCed as described above and subset directly from the SMTSD column of the annotation file to separate the substantia nigra (SN, n = 19) from non-brain regions (consisted of heart atrial appendage (HAA, n = 32),

heart left ventricle (HLV, n = 70), lung (n = 83), liver (n = 21), pancreas (n = 20), stomach (n = 31), skeletal muscle (SM, n = 123).

GTEx differential expression analysis

Prior to differential expression analysis, three groups were created: SN, OtherBrain (consisted of brain regions listed above) and NonBrain (consisted of non-brain regions listed above), then filtered for samples that have at least 10 reads total. Differential expression analysis between SN vs OtherBrain and SN vs NonBrain groups was performed using DESeq2's (v1.40.2) Wald test on the raw gene counts. Differentially expressed genes were subset for ion channels only using a predetermined list of ion channels then p-values were adjusted using the p.adjust function with the Benjamini & Hochberg (BH) method. For the top genes selected for electrical activity modulation, raw counts were z-score normalised and the mean z-score was collated to generate the expression heatmaps.

Single Cell and bulk RNA-sequencing pre-processing and quality control

Dataset pre-processing. All datasets presented in Supplementary Figure S3 were pre-processed according to previous methods[49].

Midbrain H9 Bulk RNA sequencing pre-processing. FASTQ files from bulk RNA-sequencing data were read-trimmed for paired-end reads using TrimGalore (v0.6.6) on default settings. TrimGalore quality was then assessed using FastQC on default settings. High quality trimmed reads were pseudo aligned and transcript-level abundances were quantified using Salmon (v1.10.2) with a decoy-aware transcriptome index of the *Homo Sapiens* GRCh38 genome built from human version 42 annotation on GENCODE. Trimming quality and mapped reads were summarised using MultiQC (v1.13).

Bulk RNA-sequencing visualisation. Bulk RNA sequencing datasets and associated metadata were passed through the DESeqDataSetFromMatrix function in the DESeq2 package. The estimateSizeFactors function was then used to calculate size factors for normalisation of each dataset using the median of ratios method. From here, the normalised counts were extracted from the DESeq object. Normalised data was filtered for healthy samples only and for genes of interest before graphing in GraphPad Prism 10.

Single cell RNA-sequencing visualisation. Single cells that passed quality control metrics and its associated metadata were passed through the CreateSeuratObject function from the Seurat package. Raw gene counts were then subjected to log normalisation using the NormalizeData function with assay set to 'RNA' and method set to 'LogNormalize'. Normalised gene counts were extracted using the GetAssayData function with assay set to 'RNA' and layer set to 'data'. Normalised counts were filtered for healthy samples only and for genes of interest before graphing in GraphPad Prism 10.

Single-nuclei data processing and visualisation. Post-mortem single nuclei RNA-sequencing data was accessed via the Single Cell Broad Institute (https://singlecell.broadinstitute.org/single_cell/study/SCP1768/). A matrix containing the raw gene counts, features and barcodes for each cell were loaded into R. The metadata was loaded and filtered for 'Homo sapiens' via the species__ontology_label column. Healthy and Parkinson's disease samples were filtered with the disease__ontology_label column. Cells were assigned their respective dopaminergic subpopulation as previously determined by Kamath et al. and further filtered for the SOX6-AGTR1 subpopulation. Metadata and count data were passed through CreateSeuratObject and log normalised using the NormalizeData function with assay set to 'RNA' and method set to 'LogNormalize'. Normalised counts were extracted using the GetAssayData function with assay set to 'RNA' and layer set to 'data' before graphing in GraphPad Prism 10.

Neurotoxicity Assays

For the assessment of neurotoxicity, hPSC-derived midbrain neurons were plated in 384-well CellCarrier Ultra Imaging Plates at a density of 13,000 cells/well. Neural cultures were treated as indicated. Wells were fixed and stained with DAPI, and cell culture supernatant was collected for simultaneous lactate dehydrogenase (LDH) cytotoxicity assays. LDH cytotoxicity assays were performed using a Cytotox96 Non-Radioactive Cytotoxicity Assay Kit. Cytotox96 reagent and positive control were prepared according to the manufacturer's instructions. Cytotox96 reagent was added to cell culture supernatant from neurotoxicity assays and incubated at RT for 30 minutes. Stop Solution was added following incubation and absorbance was measured at 490 nm. Fresh media was used as a negative control and all samples were tested in triplicate.

Quantification and statistical analysis

All statistical analyses were performed using R version 4.6.0 or GraphPad Prism version 11. Data are presented as mean ± SEM unless otherwise stated. Statistical tests were selected according to the experimental design and are specified in the figure legends. Statistical significance was defined as $p < 0.05$.

For experiments containing multiple technical replicates nested within independent neural differentiations, donor lines, clones or experimental batches, statistical significance was assessed using linear mixed-effects models. Linear mixed-effects models (LMMs) statistical analyses were performed in R (lme4/lmerTest). Treatment condition was modelled as a fixed effect, and the relevant biological or experimental grouping variables, such as neural differentiation, donor, clone, line or experimental batch, were modelled as random effects where appropriate. This approach was used to account for the nested structure of the data and to avoid treating technical well replicates as fully independent biological replicates. Data were normalised (when indicated in figure legends or axes) to the control mean within each biological replicate and expressed as a percentage of control. Estimated marginal means and standard errors were obtained using the emmeans package with Satterthwaite degrees of freedom. All pairwise comparisons between treatment groups were performed using Holm correction to control the familywise error rate. Model assumptions were verified by inspection of diagnostic plots and the Shapiro-Wilk test on model residuals. Data are presented as estimated marginal means ± SEM with individual well measurements and biological replicate means overlaid. White circles represent individual well replicates, and blue squares with blue paired lines represent means per independent neural differentiation.

For paired experimental designs, statistical analysis was performed in Graphpad Prism. Paired structure was incorporated into the model using the appropriate random effect or pairing factor. Where data were normalised to matched controls, statistical testing was performed on the normalised values, as specified in the figure legends. Curve fits were assessed using nonlinear least-squares regression of inhibitor concentration versus normalised response. N values are reported in the figure legends and identified as well replicates, independent neural differentiations, donor lines, clones or biological replicates, as appropriate. Biological-replicate summaries are displayed where possible to indicate reproducibility across independent differentiations or genetic backgrounds.

Mann Whitney U-tests were performed in Graphpad Prism. Where data were normalised to matched controls, statistical testing was performed on the normalised values, as specified in the figure legends.

ABBREVIATIONS

ATP	adenosine 5'-triphosphate
GTEx	genotype-tissue expression

ICM	ion channel modulators
MEA	multi-electrode array
nAChR	nicotinic acetylcholine receptor
Na_v	voltage-gated sodium channel
NMM	neuronal maturation medium
OxPhos	oxidative phosphorylation
PD	Parkinson's disease
RNA	ribonucleic acid
SN	substantia nigra
SN-ICM	substantia nigra ion channel modulators
SNpc	substantia nigra pars compacta
TH	tyrosine hydroxylase
TTX	tetrodotoxin
α-syn	alpha synuclein

957

REFERENCES

1. Cunnane, S.C., Trushina, E., Morland, C., Prigione, A., Casadesus, G., Andrews, Z.B., Beal, M.F., Bergersen, L.H., Brinton, R.D., Monte, S.d.l., et al. (2020). Brain energy rescue: an emerging therapeutic concept for neurodegenerative disorders of ageing. Nat Rev Drug Discov *19*, 1-25. 10.1038/s41573-020-0072-x.
2. Cai, R., Zhang, Y., Simmering, J.E., Schultz, J.L., Li, Y., Fernandez-Carasa, I., Consiglio, A., Raya, A., Polgreen, P.M., Narayanan, N.S., et al. (2019). Enhancing glycolysis attenuates Parkinson's disease progression in models and clinical databases. J Clin Invest *129*, 4539-4549. 10.1172/jci129987.
3. Amorim, J.A., Coppotelli, G., Rolo, A.P., Palmeira, C.M., Ross, J.M., and Sinclair, D.A. (2022). Mitochondrial and metabolic dysfunction in ageing and age-related diseases. Nat. Rev. Endocrinol. *18*, 243-258. 10.1038/s41574-021-00626-7.
4. Trigo, D., Avelar, C., Fernandes, M., Sá, J., and Silva, O.C.e. (2022). Mitochondria, energy, and metabolism in neuronal health and disease. Febs Lett *596*, 1095-1110. 10.1002/1873-3468.14298.
5. Liao, S.-C., Kano, K., Phanse, S., Nguyen, M., Margolis, E., Fu, Y., Meng, J., Moutaoufik, M.T., Chatterton, Z., Aoki, H., et al. (2024). CHCHD2 mutant mice display mitochondrial protein accumulation and disrupted energy metabolism. bioRxiv, 2024.2008.2030.610586. 10.1101/2024.08.30.610586.
6. Henrich, M.T., Oertel, W.H., Surmeier, D.J., and Geibl, F.F. (2023). Mitochondrial dysfunction in Parkinson's disease – a key disease hallmark with therapeutic potential. Mol. Neurodegener. *18*, 83. 10.1186/s13024-023-00676-7.
7. Yu, L., Jin, J., Xu, Y., and Zhu, X. (2022). Aberrant energy metabolism in Alzheimer's disease. J. Transl. Intern. Med. *10*, 197-206. 10.2478/jtim-2022-0024.
8. Singh, T., Jiao, Y., Ferrando, L.M., Yablonska, S., Li, F., Horoszko, E.C., Lacomis, D., Friedlander, R.M., and Carlisle, D.L. (2021). Neuronal mitochondrial dysfunction in sporadic amyotrophic lateral sclerosis is developmentally regulated. Sci. Rep. *11*, 18916. 10.1038/s41598-021-97928-7.
9. Coukos, R., and Krainc, D. (2024). Key genes and convergent pathogenic mechanisms in Parkinson disease. Nat. Rev. Neurosci. *25*, 393-413. 10.1038/s41583-024-00812-2.
10. McDonald, T.S., Lerskiatiphanich, T., Woodruff, T.M., McCombe, P.A., and Lee, J.D. (2022). Potential mechanisms to modify impaired glucose metabolism in neurodegenerative disorders. J. Cereb. Blood Flow Metab. *43*, 26-43. 10.1177/0271678x221135061.
11. Tran, J., Anastacio, H., and Bardy, C. (2020). Genetic predispositions of Parkinson's disease revealed in patient-derived brain cells. npj Park.'s Dis. *6*, 8. 10.1038/s41531-020-0110-8.
12. Calabresi, P., Mechelli, A., Natale, G., Volpicelli-Daley, L., Lazzaro, G.D., and Ghiglieri, V. (2023). Alpha-synuclein in Parkinson's disease and other synucleinopathies: from overt neurodegeneration back to early synaptic dysfunction. Cell Death Dis *14*, 176. 10.1038/s41419-023-05672-9.
13. Kulkarni, A., Preeti, K., Tryphena, K.P., Srivastava, S., Singh, S.B., and Khatri, D.K. (2023). Proteostasis in Parkinson's disease: Recent development and possible implication in diagnosis and therapeutics. Ageing Res. Rev. *84*, 101816. 10.1016/j.arr.2022.101816.

14. Trist, B.G., Hare, D.J., and Double, K.L. (2019). Oxidative stress in the aging substantia nigra and the etiology of Parkinson's disease. Aging Cell *18*, e13031. 10.1111/acel.13031.
15. Ni, A., and Ernst, C. (2022). Evidence That Substantia Nigra Pars Compacta Dopaminergic Neurons Are Selectively Vulnerable to Oxidative Stress Because They Are Highly Metabolically Active. Front. Cell. Neurosci. *16*, 826193. 10.3389/fncel.2022.826193.
16. Zhou, Z.D., Yi, L.X., Wang, D.Q., Lim, T.M., and Tan, E.K. (2023). Role of dopamine in the pathophysiology of Parkinson's disease. Transl. Neurodegener. *12*, 44. 10.1186/s40035-023-00378-6.
17. Janezic, S., Threlfell, S., Dodson, P.D., Dowie, M.J., Taylor, T.N., Potgieter, D., Parkkinen, L., Senior, S.L., Anwar, S., Ryan, B., et al. (2013). Deficits in dopaminergic transmission precede neuron loss and dysfunction in a new Parkinson model. Proceedings of the National Academy of Sciences *110*, E4016-E4025. 10.1073/pnas.1309143110.
18. Merino-Galán, L., Jimenez-Urbieta, H., Zamarbide, M., Rodríguez-Chinchilla, T., Belloso-Iguerategui, A., Santamaria, E., Fernández-Irigoyen, J., Aiastui, A., Doudnikoff, E., Bézard, E., et al. (2022). Striatal synaptic bioenergetic and autophagic decline in premotor experimental parkinsonism. Brain *145*, 2092-2107. 10.1093/brain/awac087.
19. Li, H., Doric, Z., Berthet, A., Jorgens, D.M., Nguyen, M.K., Hsieh, I., Margulis, J., Fang, R., Debnath, J., Sesaki, H., et al. (2021). Longitudinal tracking of neuronal mitochondria delineates PINK1/Parkin-dependent mechanisms of mitochondrial recycling and degradation. Sci. Adv. *7*, eabf6580. 10.1126/sciadv.abf6580.
20. Morris, G., Walder, K.R., Berk, M., Marx, W., Walker, A.J., Maes, M., and Puri, B.K. (2020). The interplay between oxidative stress and bioenergetic failure in neuropsychiatric illnesses: can we explain it and can we treat it? Molecular Biology Reports *47*, 5587-5620. 10.1007/s11033-020-05590-5.
21. Ottens, F., Franz, A., and Hoppe, T. (2021). Build-UPS and break-downs: metabolism impacts on proteostasis and aging. Cell Death Differ. *28*, 505-521. 10.1038/s41418-020-00682-y.
22. Kokotos, A.C., Antoniazzi, A.M., Unda, S.R., Ko, M.S., Park, D., Eliezer, D., Kaplitt, M.G., De Camilli, P., and Ryan, T.A. (2024). Phosphoglycerate kinase is a central leverage point in Parkinson's disease–driven neuronal metabolic deficits. Sci. Adv. *10*, eadn6016. doi:10.1126/sciadv.adn6016.
23. Michel, Patrick P., Hirsch, Etienne C., and Hunot, S. (2016). Understanding Dopaminergic Cell Death Pathways in Parkinson Disease. Neuron *90*, 675-691. 10.1016/j.neuron.2016.03.038.
24. Rademacher, K., Doric, Z., Haddad, D., Mamaligas, A., Liao, S.-C., Creed, R.B., Kano, K., Chatterton, Z., Fu, Y., Garcia, J.H., et al. (2024). Chronic hyperactivation of midbrain dopamine neurons causes preferential dopamine neuron degeneration. bioRxiv, 2024.2004.2005.588321. 10.1101/2024.04.05.588321.
25. Rademacher, K., and Nakamura, K. (2024). Role of dopamine neuron activity in Parkinson's disease pathophysiology. Exp. Neurol. *373*, 114645. 10.1016/j.expneurol.2023.114645.
26. Surmeier, D.J., Obeso, J.A., and Halliday, G.M. (2017). Selective neuronal vulnerability in Parkinson disease. Nat. Rev. Neurosci. *18*, 101-113. 10.1038/nrn.2016.178.
27. Engl, E., and Attwell, D. (2015). Non-signalling energy use in the brain. J Physiology *593*, 3417-3429. 10.1113/jphysiol.2014.282517.
28. Harris, Julia J., Jolivet, R., and Attwell, D. (2012). Synaptic Energy Use and Supply. Neuron *75*, 762-777. 10.1016/j.neuron.2012.08.019.

29. Li, S., and Sheng, Z.-H. (2022). Energy matters: presynaptic metabolism and the maintenance of synaptic transmission. Nat. Rev. Neurosci. *23*, 4-22. 10.1038/s41583-021-00535-8.
30. Attwell, D., and Laughlin, S.B. (2001). An Energy Budget for Signaling in the Grey Matter of the Brain. J. Cereb. Blood Flow Metab. *21*, 1133-1145. 10.1097/00004647-200110000-00001.
31. Pacelli, C., Giguère, N., Bourque, M.-J., Lévesque, M., Slack, Ruth S., and Trudeau, L.-É. (2015). Elevated Mitochondrial Bioenergetics and Axonal Arborization Size Are Key Contributors to the Vulnerability of Dopamine Neurons. Curr Biol *25*, 2349-2360. 10.1016/j.cub.2015.07.050.
32. Hallermann, S., Kock, C.P.J.d., Stuart, G.J., and Kole, M.H.P. (2012). State and location dependence of action potential metabolic cost in cortical pyramidal neurons. Nat. Neurosci. *15*, 1007-1014. 10.1038/nn.3132.
33. Carter, B.C., and Bean, B.P. (2009). Sodium Entry during Action Potentials of Mammalian Neurons: Incomplete Inactivation and Reduced Metabolic Efficiency in Fast-Spiking Neurons. Neuron *64*, 898-909. 10.1016/j.neuron.2009.12.011.
34. Hasenstaub, A., Otte, S., Callaway, E., and Sejnowski, T.J. (2010). Metabolic cost as a unifying principle governing neuronal biophysics. Proceedings of the National Academy of Sciences *107*, 12329-12334. 10.1073/pnas.0914886107.
35. Sulzer, D., Cragg, S.J., and Rice, M.E. (2016). Striatal dopamine neurotransmission: Regulation of release and uptake. Basal Ganglia *6*, 123-148. 10.1016/j.baga.2016.02.001.
36. Ashrafi, G., Juan-Sanz, J.d., Farrell, R.J., and Ryan, T.A. (2020). Molecular Tuning of the Axonal Mitochondrial Ca2+ Uniporter Ensures Metabolic Flexibility of Neurotransmission. Neuron *105*, 678-687.e675. 10.1016/j.neuron.2019.11.020.
37. Rey, N.L.-G.d., Hernández-Pinedo, N., Carrillo, M., Cerro, M.d., Esteban-García, N., Trigo-Damas, I., Monje, M.H.G., Lanciego, J.L., Cavada, C., Obeso, J.A., and Blesa, J. (2024). Calbindin and Girk2/Aldh1a1 define resilient vs vulnerable dopaminergic neurons in a primate Parkinson's disease model. npj Park.'s Dis. *10*, 165. 10.1038/s41531-024-00777-0.
38. Muddapu, V.R., Dharshini, S.A.P., Chakravarthy, V.S., and Gromiha, M.M. (2020). Neurodegenerative Diseases - Is Metabolic Deficiency the Root Cause? Front Neurosci-switz *14*, 213. 10.3389/fnins.2020.00213.
39. Muddapu, V.R., Mandali, A., Chakravarthy, V.S., and Ramaswamy, S. (2019). A Computational Model of Loss of Dopaminergic Cells in Parkinson's Disease Due to Glutamate-Induced Excitotoxicity. Front Neural Circuit *13*, 11. 10.3389/fncir.2019.00011.
40. Pissadaki, E.K., and Bolam, J.P. (2013). The energy cost of action potential propagation in dopamine neurons: clues to susceptibility in Parkinson's disease. Front Comput Neurosc *7*, 13. 10.3389/fncom.2013.00013.
41. Zampese, E., Wokosin, D.L., Gonzalez-Rodriguez, P., Guzman, J.N., Tkatch, T., Kondapalli, J., Surmeier, W.C., D'Alessandro, K.B., Stefani, D.D., Rizzuto, R., et al. (2022). Ca2+ channels couple spiking to mitochondrial metabolism in substantia nigra dopaminergic neurons. Sci. Adv. *8*, eabp8701. 10.1126/sciadv.abp8701.
42. Dorsey, E.R., and Bloem, B.R. (2024). Parkinson's Disease Is Predominantly an Environmental Disease. J. Park.'s Dis. *14*, 451-465. 10.3233/jpd-230357.
43. Lim, S.-Y., and Klein, C. (2024). Parkinson's Disease is Predominantly a Genetic Disease. J. Park.'s Dis. *14*, 467-482. 10.3233/jpd-230376.
44. Doric, Z., Li, H., and Nakamura, K. (2022). The PINK1 advantage: recycling mitochondria in times of trouble? Autophagy *18*, 231-232. 10.1080/15548627.2021.1998872.

45. Bardy, C., Hurk, M.v.d., Eames, T., Marchand, C., Hernandez, R.V., Kellogg, M., Gorris, M., Galet, B., Palomares, V., Brown, J., et al. (2015). Neuronal medium that supports basic synaptic functions and activity of human neurons in vitro. Proceedings of the National Academy of Sciences *112*, E2725-E2734. 10.1073/pnas.1504393112.
46. Milky, B., Zabolocki, M., Al-Bataineh, S.A., Hurk, M.v.d., Greenberg, Z., Turner, L., Mazzachi, P., Williams, A., Illeperuma, I., Adams, R., et al. (2022). Long-term adherence of human brain cells in vitro is enhanced by charged amine-based plasma polymer coatings. Stem Cell Rep. *17*, 489-506. 10.1016/j.stemcr.2022.01.013.
47. Bardy, C., Hurk, M.v.d., Kakaradov, B., Erwin, J.A., Jaeger, B.N., Hernandez, R.V., Eames, T., Paucar, A.A., Gorris, M., Marchand, C., et al. (2016). Predicting the functional states of human iPSC-derived neurons with single-cell RNA-seq and electrophysiology. Mol. Psychiatry *21*, 1573-1588. 10.1038/mp.2016.158.
48. Carosi, J.M., Hein, L.K., Hurk, M.v.d., Adams, R., Milky, B., Singh, S., Bardy, C., Denton, D., Kumar, S., and Sargeant, T.J. (2021). Retromer regulates the lysosomal clearance of MAPT/tau. Autophagy *17*, 2217-2237. 10.1080/15548627.2020.1821545.
49. Hurk, M.v.d., Lau, S., Marchetto, M.C., Mertens, J., Stern, S., Corti, O., Brice, A., Winner, B., Winkler, J., Gage, F.H., and Bardy, C. (2022). Druggable transcriptomic pathways revealed in Parkinson's patient-derived midbrain neurons. npj Park.'s Dis. *8*, 134. 10.1038/s41531-022-00400-0.
50. Lam, W.K., Lindblom, R.S.J., Milky, B., Mazzachi, P., Hadian-Jazi, M., Küng, C., Khuu, G., Uoselis, L., Nguyen, T.N., Skulsuppaisarn, M., et al. (2024). Presynapses are mitophagy pit stops that prevent axon degeneration. bioRxiv, 2024.2009.2009.611943. 10.1101/2024.09.09.611943.
51. Innos, J., and Hickey, M.A. (2021). Using Rotenone to Model Parkinson's Disease in Mice: A Review of the Role of Pharmacokinetics. Chem Res Toxicol *34*, 1223-1239. 10.1021/acs.chemrestox.0c00522.
52. Baeza-Lehnert, F., Saab, A.S., Gutiérrez, R., Larenas, V., Díaz, E., Horn, M., Vargas, M., Hösli, L., Stobart, J., Hirrlinger, J., et al. (2019). Non-Canonical Control of Neuronal Energy Status by the Na+ Pump. Cell Metab. *29*, 668-680.e664. 10.1016/j.cmet.2018.11.005.
53. Kamath, T., Abdulraouf, A., Burris, S.J., Langlieb, J., Gazestani, V., Nadaf, N.M., Balderrama, K., Vanderburg, C., and Macosko, E.Z. (2022). Single-cell genomic profiling of human dopamine neurons identifies a population that selectively degenerates in Parkinson's disease. Nat. Neurosci. *25*, 588-595. 10.1038/s41593-022-01061-1.
54. Dong-Chen, X., Yong, C., Yang, X., Chen-Yu, S., and Li-Hua, P. (2023). Signaling pathways in Parkinson's disease: molecular mechanisms and therapeutic interventions. Signal Transduct. Target. Ther. *8*, 73. 10.1038/s41392-023-01353-3.
55. Zhang, S., Wang, R., and Wang, G. (2019). Impact of Dopamine Oxidation on Dopaminergic Neurodegeneration. ACS Chem. Neurosci. *10*, 945-953. 10.1021/acschemneuro.8b00454.
56. Navarro-Yepes, J., Burns, M., Anandhan, A., Khalimonchuk, O., Razo, L.M.d., Quintanilla-Vega, B., Pappa, A., Panayiotidis, M.I., and Franco, R. (2014). Oxidative Stress, Redox Signaling, and Autophagy: Cell Death Versus Survival. Antioxid. Redox Signal. *21*, 66-85. 10.1089/ars.2014.5837.
57. Petit, P., Berger, F., Bonneterre, V., and Vuillerme, N. (2025). Investigating Parkinson's disease risk across farming activities using data mining and large-scale administrative health data. NPJ Parkinsons Dis *11*, 13. 10.1038/s41531-024-00864-2.
58. Domingo, A., and Klein, C. (2018). Chapter 14 Genetics of Parkinson disease. Handb. Clin. Neurol. *147*, 211-227. 10.1016/b978-0-444-63233-3.00014-2.

59. Park, J.-S., Davis, R.L., and Sue, C.M. (2018). Mitochondrial Dysfunction in Parkinson's Disease: New Mechanistic Insights and Therapeutic Perspectives. Curr Neurol Neurosci *18*, 21. 10.1007/s11910-018-0829-3.
60. Bogetofte, H., Jensen, P., Ryding, M., Schmidt, S.I., Okarmus, J., Ritter, L., Worm, C.S., Hohnholt, M.C., Azevedo, C., Roybon, L., et al. (2019). PARK2 Mutation Causes Metabolic Disturbances and Impaired Survival of Human iPSC-Derived Neurons. Front. Cell. Neurosci. *13*, 297. 10.3389/fncel.2019.00297.
61. Shaltouki, A., Sivapatham, R., Pei, Y., Gerencser, Akos A., Momčilović, O., Rao, Mahendra S., and Zeng, X. (2015). Mitochondrial Alterations by PARKIN in Dopaminergic Neurons Using PARK2 Patient-Specific and PARK2 Knockout Isogenic iPSC Lines. Stem Cell Rep. *4*, 847-859. 10.1016/j.stemcr.2015.02.019.
62. Pantazis, C.B., Yang, A., Lara, E., McDonough, J.A., Blauwendraat, C., Peng, L., Oguro, H., Kanaujiya, J., Zou, J., Sebesta, D., et al. (2022). A reference human induced pluripotent stem cell line for large-scale collaborative studies. Cell Stem Cell *29*, 1685-1702.e1622. 10.1016/j.stem.2022.11.004.
63. McFarthing, K., Buff, S., Rafaloff, G., Pitzer, K., Fiske, B., Navangul, A., Beissert, K., Pilcicka, A., Fuest, R., Wyse, R.K., and Stott, S.R.W. (2024). Parkinson's Disease Drug Therapies in the Clinical Trial Pipeline: 2024 Update. J. Park.'s Dis. *14*, 899-912. 10.3233/jpd-240272.
64. Kordower, J.H., Olanow, C.W., Dodiya, H.B., Chu, Y., Beach, T.G., Adler, C.H., Halliday, G.M., and Bartus, R.T. (2013). Disease duration and the integrity of the nigrostriatal system in Parkinson's disease. Brain *136*, 2419-2431. 10.1093/brain/awt192.
65. Sloan, M., Alegre-Abarrategui, J., Potgieter, D., Kaufmann, A.-K., Exley, R., Deltheil, T., Threlfell, S., Connor-Robson, N., Brimblecombe, K., Wallings, R., et al. (2016). LRRK2 BAC transgenic rats develop progressive, L-DOPA-responsive motor impairment, and deficits in dopamine circuit function. Hum Mol Genet *25*, 951-963. 10.1093/hmg/ddv628.
66. Pathak, D., Shields, L.Y., Mendelsohn, B.A., Haddad, D., Lin, W., Gerencser, A.A., Kim, H., Brand, M.D., Edwards, R.H., and Nakamura, K. (2015). The Role of Mitochondrially Derived ATP in Synaptic Vesicle Recycling* ♦. J. Biol. Chem. *290*, 22325-22336. 10.1074/jbc.m115.656405.
67. Rangaraju, V., Calloway, N., and Ryan, Timothy A. (2014). Activity-Driven Local ATP Synthesis Is Required for Synaptic Function. Cell *156*, 825-835. 10.1016/j.cell.2013.12.042.
68. Tzioras, M., McGeachan, R.I., Durrant, C.S., and Spires-Jones, T.L. (2023). Synaptic degeneration in Alzheimer disease. Nat. Rev. Neurol. *19*, 19-38. 10.1038/s41582-022-00749-z.
69. Bero, A.W., Yan, P., Roh, J.H., Cirrito, J.R., Stewart, F.R., Raichle, M.E., Lee, J.-M., and Holtzman, D.M. (2011). Neuronal activity regulates the regional vulnerability to amyloid-β deposition. Nat. Neurosci. *14*, 750-756. 10.1038/nn.2801.
70. Wu, J.W., Hussaini, S.A., Bastille, I.M., Rodriguez, G.A., Mrejeru, A., Rilett, K., Sanders, D.W., Cook, C., Fu, H., Boonen, R.A.C.M., et al. (2016). Neuronal activity enhances tau propagation and tau pathology in vivo. Nat. Neurosci. *19*, 1085-1092. 10.1038/nn.4328.
71. Herrero-Mendez, A., Almeida, A., Fernández, E., Maestre, C., Moncada, S., and Bolaños, J.P. (2009). The bioenergetic and antioxidant status of neurons is controlled by continuous degradation of a key glycolytic enzyme by APC/C–Cdh1. Nat Cell Biol *11*, 747-752. 10.1038/ncb1881.
72. Zheng, X., Boyer, L., Jin, M., Kim, Y., Fan, W., Bardy, C., Berggren, T., Evans, R.M., Gage, F.H., and Hunter, T. (2016). Alleviation of neuronal energy deficiency by mTOR inhibition as a treatment for mitochondria-related neurodegeneration. eLife *5*, e13378. 10.7554/elife.13378.

73. Filomeni, G., Zio, D.D., and Cecconi, F. (2015). Oxidative stress and autophagy: the clash between damage and metabolic needs. Cell Death Differ. *22*, 377-388. 10.1038/cdd.2014.150.
74. Lazarou, M., Sliter, D.A., Kane, L.A., Sarraf, S.A., Wang, C., Burman, J.L., Sideris, D.P., Fogel, A.I., and Youle, R.J. (2015). The ubiquitin kinase PINK1 recruits autophagy receptors to induce mitophagy. Nature *524*, 309-314. 10.1038/nature14893.
75. Hommen, F., Bilican, S., and Vilchez, D. (2022). Protein clearance strategies for disease intervention. J. Neural Transmission *129*, 141-172. 10.1007/s00702-021-02431-y.
76. Mandic, M., Paunovic, V., Vucicevic, L., Kosic, M., Mijatovic, S., Trajkovic, V., and Harhaji-Trajkovic, L. (2024). No energy, no autophagy—Mechanisms and therapeutic implications of autophagic response energy requirements. J. Cell. Physiol. *239*, e31366. 10.1002/jcp.31366.
77. Im, E., Jiang, Y., Stavrides, P.H., Darji, S., Erdjument-Bromage, H., Neubert, T.A., Choi, J.Y., Wegiel, J., Lee, J.-H., and Nixon, R.A. (2023). Lysosomal dysfunction in Down syndrome and Alzheimer mouse models is caused by v-ATPase inhibition by Tyr682-phosphorylated APP βCTF. Sci. Adv. *9*, eadg1925. 10.1126/sciadv.adg1925.
78. Nixon, R.A., and Rubinsztein, D.C. (2024). Mechanisms of autophagy–lysosome dysfunction in neurodegenerative diseases. Nat. Rev. Mol. Cell Biol. *25*, 1-21. 10.1038/s41580-024-00757-5.
79. Nguyen, H.N., Byers, B., Cord, B., Shcheglovitov, A., Byrne, J., Gujar, P., Kee, K., Schule, B., Dolmetsch, R.E., Langston, W., et al. (2011). LRRK2 mutant iPSC-derived DA neurons demonstrate increased susceptibility to oxidative stress. Cell Stem Cell *8*, 267-280. 10.1016/j.stem.2011.01.013.
80. Morais, V.A., Verstreken, P., Roethig, A., Smet, J., Snellinx, A., Vanbrabant, M., Haddad, D., Frezza, C., Mandemakers, W., Vogt-Weisenhorn, D., et al. (2009). Parkinson's disease mutations in PINK1 result in decreased Complex I activity and deficient synaptic function. EMBO Mol Med *1*, 99-111. 10.1002/emmm.200900006.
81. Gautier, C.A., Kitada, T., and Shen, J. (2008). Loss of PINK1 causes mitochondrial functional defects and increased sensitivity to oxidative stress. Proc Natl Acad Sci U S A *105*, 11364-11369. 10.1073/pnas.0802076105.
82. Holford, M., Daly, M., King, G.F., and Norton, R.S. (2018). Venoms to the rescue. Science *361*, 842-844. 10.1126/science.aau7761.
83. Muttenthaler, M., King, G.F., Adams, D.J., and Alewood, P.F. (2021). Trends in peptide drug discovery. Nat Rev Drug Discov *20*, 309-325. 10.1038/s41573-020-00135-8.
84. Lebbe, E.K.M., Peigneur, S., Wijesekara, I., and Tytgat, J. (2014). Conotoxins Targeting Nicotinic Acetylcholine Receptors: An Overview. Mar. Drugs *12*, 2970-3004. 10.3390/md12052970.
85. Xie, T., Qin, Y., Zhao, J., Dong, J., Qi, P., Zhang, P., Zhangsun, D., Zhu, X., Yu, J., and Luo, S. (2023). Molecular Determinants of Species Specificity of α-Conotoxin TxIB towards Rat and Human α6/α3β4 Nicotinic Acetylcholine Receptors. International Journal of Molecular Sciences *24*, 8618. 10.3390/ijms24108618.
86. Kozek, K.A., Du, Y., Sharma, S., Prael, F.J., Spitznagel, B.D., Kharade, S.V., Denton, J.S., Hopkins, C.R., and Weaver, C.D. (2019). Discovery and Characterization of VU0529331, a Synthetic Small-Molecule Activator of Homomeric G Protein-Gated, Inwardly Rectifying, Potassium (GIRK) Channels. ACS Chem. Neurosci. *10*, 358-370. 10.1021/acschemneuro.8b00287.
87. Abbruzzese, G., Barone, P., Lopiano, L., and Stocchi, F. (2021). The Current Evidence for the Use of Safinamide for the Treatment of Parkinson's Disease. Drug Des., Dev. Ther. *15*, 2507-2517. 10.2147/dddt.s302673.
88. Espinoza-Vinces, C., Villino-Rodríguez, R., Atorrasagasti-Villar, A., Martí-Andrés, G., and Luquin, M.-R. (2023). Impact of Safinamide on Patient-Reported Outcomes in

Parkinson's Disease. Patient Relat. Outcome Meas. *14*, 285-295. 10.2147/prom.s369590.

89. Hung, T.-Y., Wu, S.-N., and Huang, C.-W. (2024). Safinamide, an inhibitor of monoamine oxidase, modulates the magnitude, gating, and hysteresis of sodium ion current. BMC Pharmacol. Toxicol. *25*, 17. 10.1186/s40360-024-00739-5.
90. Sciaccaluga, M., Mazzocchetti, P., Bastioli, G., Ghiglieri, V., Cardinale, A., Mosci, P., Caccia, C., Keywood, C., Melloni, E., Padoani, G., et al. (2020). Effects of safinamide on the glutamatergic striatal network in experimental Parkinson's disease. Neuropharmacology *170*, 108024. 10.1016/j.neuropharm.2020.108024.
91. Santos, R., Ursu, O., Gaulton, A., Bento, A.P., Donadi, R.S., Bologa, C.G., Karlsson, A., Al-Lazikani, B., Hersey, A., Oprea, T.I., and Overington, J.P. (2017). A comprehensive map of molecular drug targets. Nat Rev Drug Discov *16*, 19-34. 10.1038/nrd.2016.230.
92. Lachenmayer, M.L., Mürset, M., Antih, N., Debove, I., Muellner, J., Bompart, M., Schlaeppi, J.-A., Nowacki, A., You, H., Michelis, J.P., et al. (2021). Subthalamic and pallidal deep brain stimulation for Parkinson's disease—meta-analysis of outcomes. npj Park.'s Dis. *7*, 77. 10.1038/s41531-021-00223-5.
93. Boyer, L.F., Campbell, B., Larkin, S., Mu, Y., and Gage, F.H. (2012). Dopaminergic Differentiation of Human Pluripotent Cells. Curr. Protoc. Stem Cell Biol. *22*, 1H.6.1-1H.6.11. 10.1002/9780470151808.sc01h06s22.
94. Repina, N.A., Johnson, H.J., McClave, T., Kane, R.S., and Schaffer, D.V. (2020). Protocol to Fabricate Engineered Illumination Devices for Optogenetic Control of Cellular Signaling Dynamics. STAR Protoc. *1*, 100141. 10.1016/j.xpro.2020.100141.
95. Mazzachi, P., McDonald, E., Greenberg, Z., Puerta, A.N., Tran, J., De Silva, M.I., Christensen, C., Adams, R., Loskarn, S., Beard, H., et al. (2026). Modelling synaptic dysfunction in childhood dementia using human iPSC-derived cortical networks. Nature Communications *17*, 3161. 10.1038/s41467-026-71112-9.
96. Hassiotis, S., Manavis, J., Blumbergs, P.C., Hattersley, K.J., Carosi, J.M., Kamei, M., and Sargeant, T.J. (2018). Lysosomal LAMP1 immunoreactivity exists in both diffuse and neuritic amyloid plaques in the human hippocampus. Eur. J. Neurosci. *47*, 1043-1053. 10.1111/ejn.13913.
97. Meikle, P.J., Grasby, D.J., Dean, C.J., Lang, D.L., Bockmann, M., Whittle, A.M., Fietz, M.J., Simonsen, H., Fuller, M., Brooks, D.A., and Hopwood, J.J. (2006). Newborn screening for lysosomal storage disorders. Mol. Genet. Metab. *88*, 307-314. 10.1016/j.ymgme.2006.02.013.

Transient reduction of neuronal electrical activity replenishes energy levels and protects PARK2 patient-derived neurons against oxidative stress

Fig 1. Generation of functional human midbrain neuronal cultures enriched for dopaminergic features.

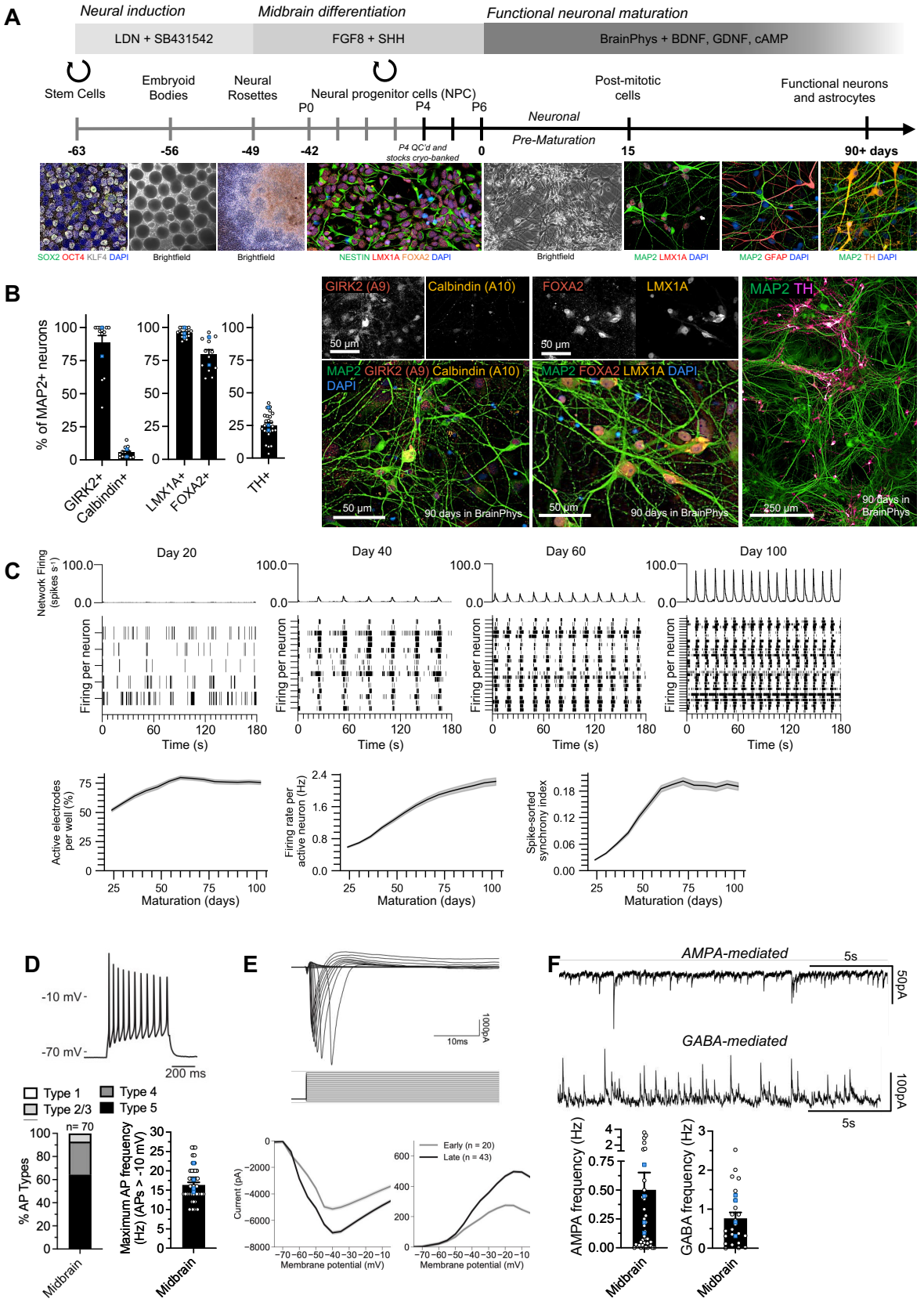


Figure 1. Generation of functional human midbrain neural cultures enriched for substantia nigra features. (**A**) Schematic depicting the neural induction, midbrain differentiation and maturation timeline used to generate neural cultures from human stem cells. Grey bars indicate growth factors supplied during the three phases: neural induction, LDN-193189 and SB431542; midbrain differentiation, FGF8 (fibroblast growth factor 8) and SHH (sonic hedgehog); and functional neuronal maturation, BDNF (brain-derived neurotrophic factor), GDNF (glia-derived neurotrophic factor) and cAMP (cyclic adenosine monophosphate). P# indicates passage number. QC indicates the time point at which quality-control measures were performed, as detailed in the Methods. Images illustrate the sequential progression from stem cells to embryoid bodies, neural rosettes, neural progenitor cells and mature neural cultures containing astrocytes and dopaminergic neurons. SOX2, OCT4 and KLF4 expression indicates stem cell pluripotency. NESTIN, LMX1A and FOXA2 expression marks neural progenitor and midbrain patterning. MAP2 and LMX1A expression indicates the development of midbrain-patterned neurons. GFAP indicates astrocytes, and TH indicates dopaminergic neurons. (**B**) Neuronal identity of 90-day-mature cultures assessed by immunocytochemical analysis of MAP2, GIRK2, calbindin and TH expression. Bars represent mean ± SEM. White circles represent individual well replicates, and blue squares represent the mean per independent neural differentiation (n = 2-3). (**C**) Multi-electrode array (MEA) extracellular recordings of neuronal electrical activity. Representative 180s raster plots depict action potential firing of individual neurons from day 20 to day 100 of maturation. Associated line graphs indicate firing density within synchronous network events. Each plot depicts a single well. Each row depicts a single neuron. Each vertical line depicts an action potential. Time-series graphs show maturation of neuronal network activity between days 25 and 100, measured by the number of active neurons per well (>5 spikes per minute), firing rate of active neurons (Hz), and synchrony index per well. Lines depict the mean of 29 wells across three independent neural differentiations, and shaded areas indicate ± SEM. (**D-F**) Whole-cell patch-clamp recordings of neuronal activity. (**D**) In current-clamp mode, neurons were held at −70 mV and injected with incremental current steps to evoke action potentials. Only highly functional Type 5 neurons[47] were analysed in panels E-F. Representative trace shows action potential firing from midbrain neural cultures. Long-term maturation of midbrain neural cultures produced mostly Type 5 neurons, which are capable of repetitive action potential firing. White circles represent individual patched neurons (n = 45), and blue squares represent the mean for each independent neural differentiation (n = 4). (**E**) Representative trace of voltage-gated sodium and potassium channel function. Activation curves for voltage-gated sodium channels (left) and potassium channels (right) are shown for early (≤61 days in culture) and late (≥92 days in culture) time points, indicating functional channel activity. (**F**) Representative traces of AMPA-mediated (top) and GABA-mediated (bottom) spontaneous postsynaptic communication. AMPA and GABA event frequency indicate that Type 5 midbrain neurons develop functional synapses. White circles represent individual patched neurons (n = 42 for AMPA; n = 23 for GABA), and blue squares represent the mean for each independent neural differentiation (n = 4 for both).

Fig 2. Transient blocking of neuronal electrical activity by generic ion channel modulators raises ATP levels

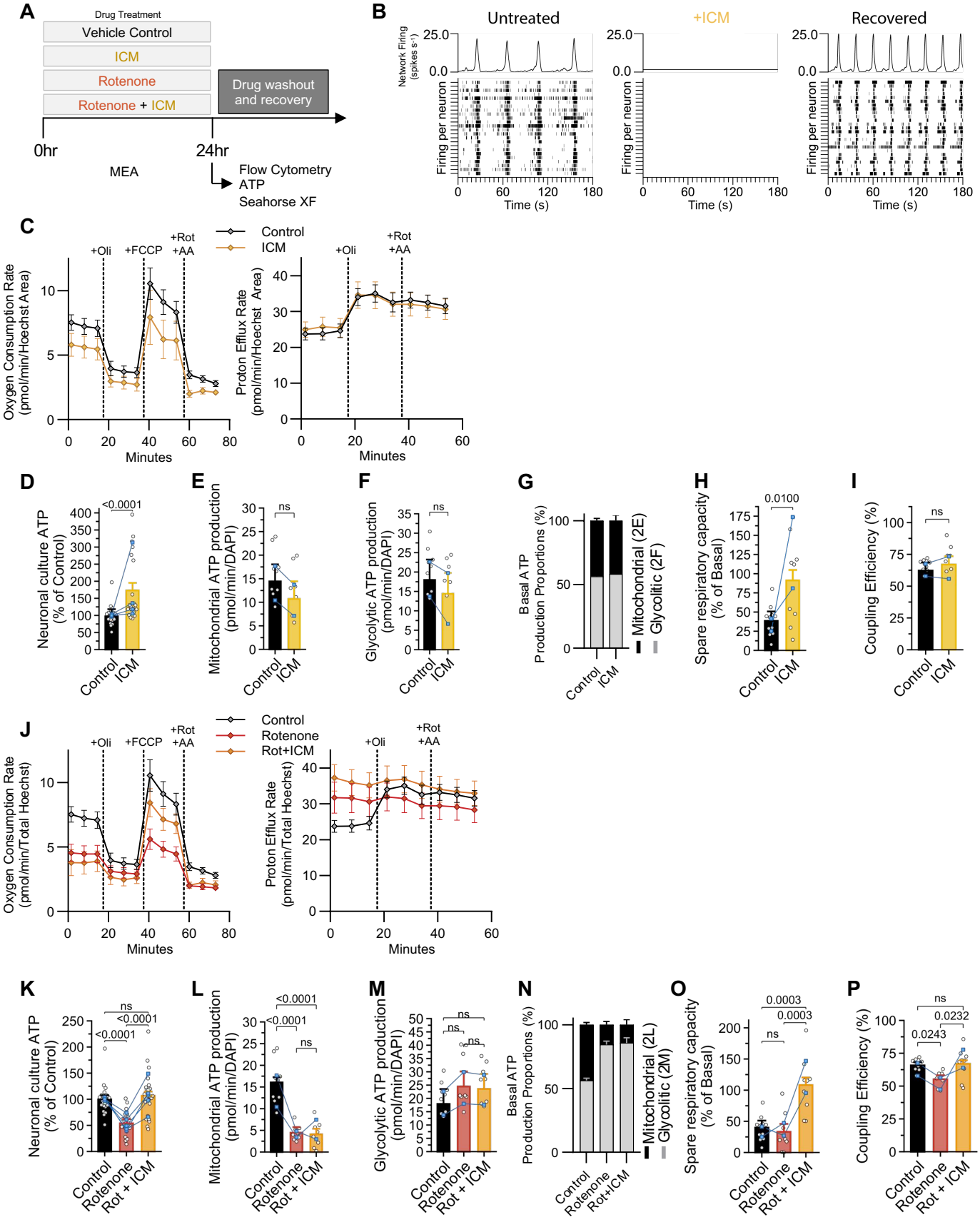


Figure 2. Transient blockade of neuronal electrical activity by generic ion channel modulators raises ATP levels.

(**A**) Schematic depicting the treatment timeline for exposure of midbrain neural cultures to treatments and downstream analyses. (**B**) Representative 180-s raster plots depicting action potential firing of individual neurons before treatment, during 24h exposure to a cocktail of ion channel modulators (ICMs; 1 μM tetrodotoxin, 10 μM NBQX, 10 μM APV), and after recovery following drug washout (336 h post-washout). Associated line graphs indicate firing density within synchronous network events, measured as spikes per second. Each plot depicts a single well. Each row depicts a single neuron. Each vertical line depicts an action potential. (**C and J**) Oxygen consumption rate (left) and proton efflux rate (right) kinetic traces from Seahorse XF Mito Stress Test and Real-Time ATP Rate assays. Data points represent the mean ± SEM. Respective graphs across 2C and 2J display the same control data. (**D**) ATP levels measured from lysates of cultures exposed to vehicle control or the ICM cocktail for 24 h. Bars represent mean ± SEM (n = 4 independent neural differentiations). Data were normalised to the vehicle control. (**E-I**) Seahorse XF measurements of culture bioenergetics after 24h exposure to vehicle or ICMs using Mito Stress Test and Real-Time ATP Rate assays. Bars represent mean ± SEM (n = 2 independent neural differentiations). In (**G**), E and F are combined into total cellular ATP production, normalised to 100% and partitioned into the proportion derived from glycolysis and the proportion derived from mitochondrial respiration. Data displayed is the same as in E and F. (**K**) ATP levels measured from lysates of cultures exposed for 24h to vehicle control, rotenone at the concentration corresponding to a 50% reduction in ATP levels for each neural batch (IC50), or co-exposure to rotenone and ICMs. Bars represent mean ± SEM (n = 5 independent neural differentiations). Data were normalised to the mean of the vehicle control. Four data points of the control data are the same as in Figure 2D. (**L-P**) Seahorse XF measurements of culture bioenergetics after 24h exposure to vehicle, rotenone, or rotenone plus ICMs. Bars represent mean ± SEM (n = 2 independent neural differentiations). Control data are the same as respective graphs in Figures 2E-I. In (**N**), L and M are combined into total cellular ATP production, normalised to 100% and partitioned into the proportion derived from glycolysis and the proportion derived from mitochondrial respiration. Data displayed is the same as in L and M. (**D-I, K-P**) White circles represent individual well replicates, and blue squares with blue paired lines represent means per independent neural differentiation (n = 2-5). Statistical significance was determined using linear mixed-effects models, as described in the Methods. See also Supplementary Figure S1.

Fig 3. Optogenetic inhibition of electrophysiological activity restores ATP levels in midbrain neurons with impaired mitochondria

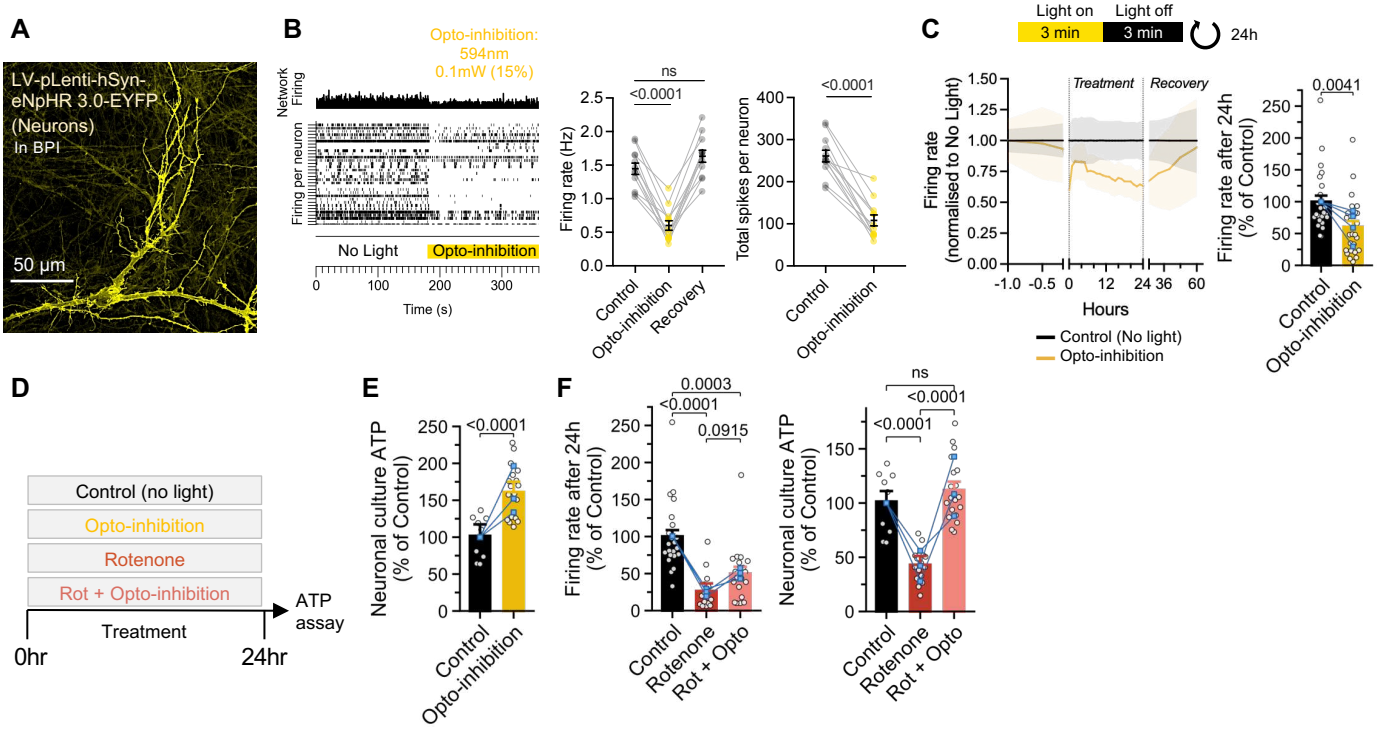


Figure 3. Optogenetic inhibition of neuronal electrical activity restores ATP levels in midbrain neurons with impaired mitochondria.

(**A**) Representative confocal image of halorhodopsin (eNpHR3.0-EYFP) expression in a neuron, captured in BrainPhys Imaging culture medium (BPI). (**B**) Representative 360s raster plots depicting action potential firing of individual halorhodopsin-expressing neurons, including 180s of optical stimulation at 594 nm, indicated by the yellow bar. Line graphs show neuronal electrical activity parameters, including firing rate (left) and total spikes per neuron (right), before, during and after light stimulation. Each line represents one neuron (n = 12 neurons). Error bars indicate mean ± SEM. Statistical significance determined using a one-way ANOVA with Dunnet's multiple comparison (left) or Wilcoxon test (right). (**C**) Time-series graph showing firing rate of active neurons in cultures with optogenetic inhibition and in control cultures that were expressing halorhodopsin but received no light stimulation. Optical stimulation consisted of a 3-min-on, 3-min-off repeating pattern for 24h. Lines depict the mean change from the first pre-treatment recording, normalised to control, from n = 4 independent neural differentiations. The bar graph shows firing rate after 24h of optogenetic inhibition. Data are normalised to the mean of the control condition. (**D**) Schematic depicting the treatment and light-stimulation timeline for panels E-F. (**E**) ATP levels measured from lysates of cultures exposed to control conditions or 24h of optogenetic inhibition. Data were normalised to the matched control condition that received no optogenetic light stimulation (n = 3 independent neural differentiations). (**F**) Firing rate and ATP levels measured from cultures exposed to vehicle control, rotenone at the concentration corresponding to a 50% reduction in ATP levels for each neural differentiation, or co-exposure to rotenone and optogenetic inhibition for 24 h. Data were normalised to the mean of the control condition (n = 3 independent neural differentiations). (**C, E-F**) White circles represent individual well replicates, and blue squares with blue paired lines represent means per independent neural differentiation. Bars and shaded areas represent mean ± SEM. Statistical significance was determined using linear mixed-effects models, as described in the Methods. See also Supplementary Figure S2.

Fig 4. Ion channels with higher expression in human midbrain SN neurons

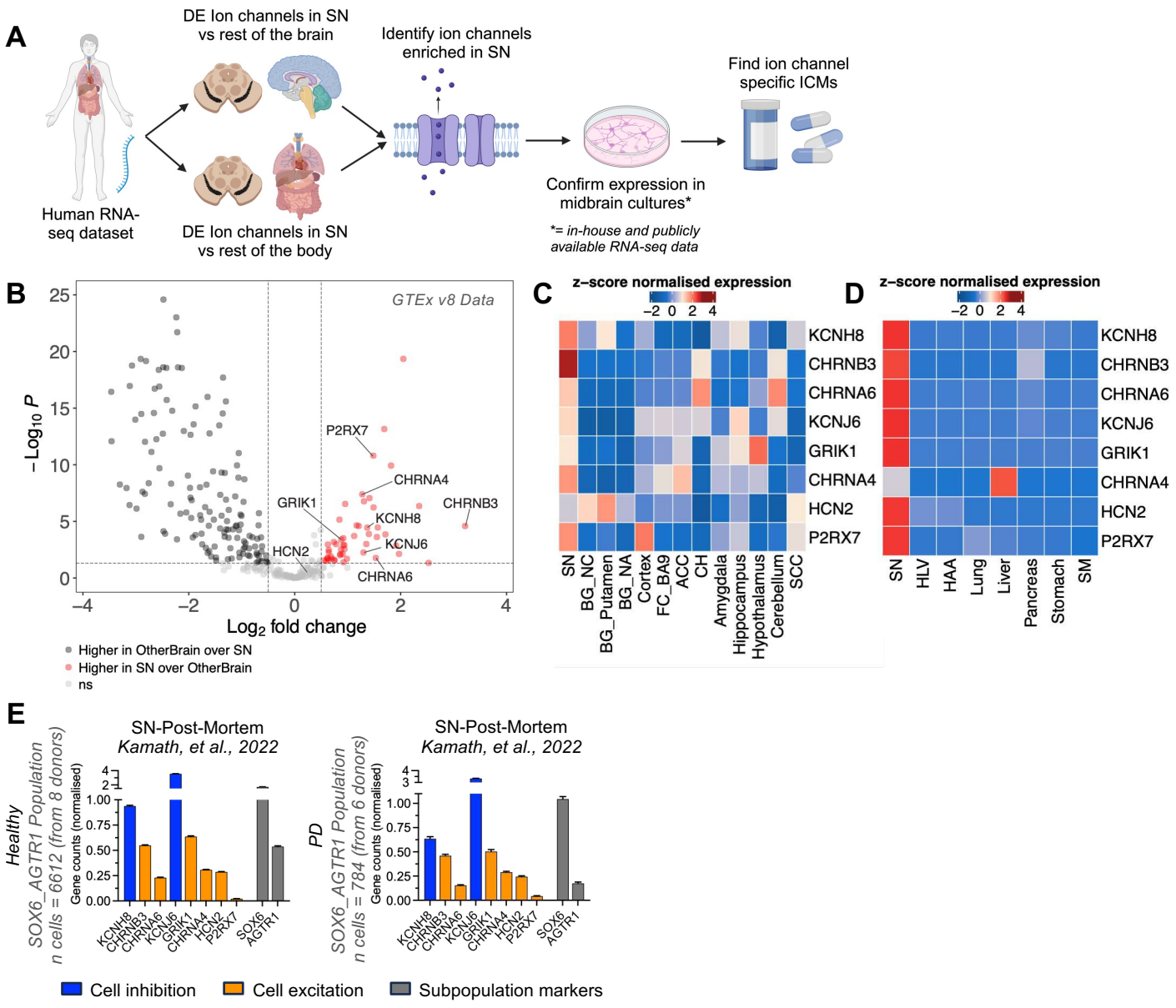


Figure 4. Ion channels with higher expression in human midbrain substantia nigra neurons.

(**A**) Schematic summarising the strategy used to select target ion channels for modulation of midbrain neuronal activity. (**B**) Volcano plot showing ion channels differentially expressed between the substantia nigra and other brain regions. Red points indicate channels significantly upregulated in the substantia nigra, black points indicate channels significantly upregulated in other brain regions, and grey points indicate channels that are not significantly differentially expressed. Labelled genes indicate channels selected for targeting with specific ICMs. (**C**) Heatmap showing expression of the eight selected channels in the substantia nigra relative to other brain regions. SN, substantia nigra; BG, basal ganglia; BG_NC, basal ganglia caudate nucleus; FC_BA9, frontal cortex BA9 region; ACC, anterior cingulate cortex; CH, cerebellar hemisphere; SCC, spinal cord cervical. (**D**) Heatmap showing expression of the eight selected channels in the substantia nigra relative to other tissues. SN, substantia nigra; HLV, heart left ventricle; HAA, heart atrial appendage; SM, skeletal muscle. (**E**) Expression of selected channels in a previously identified subpopulation of dopaminergic neurons vulnerable to degeneration in PD[53]. Bar colours indicate whether each channel is associated with cellular excitation (orange) or inhibition (blue), or identifies markers of the vulnerable dopaminergic neuron subpopulation (grey). See also Supplementary Figure S3.

Fig 5. Substantia Nigra-enriched ICMs reduce electrical activity of human midbrain neurons and enhance neuronal ATP levels

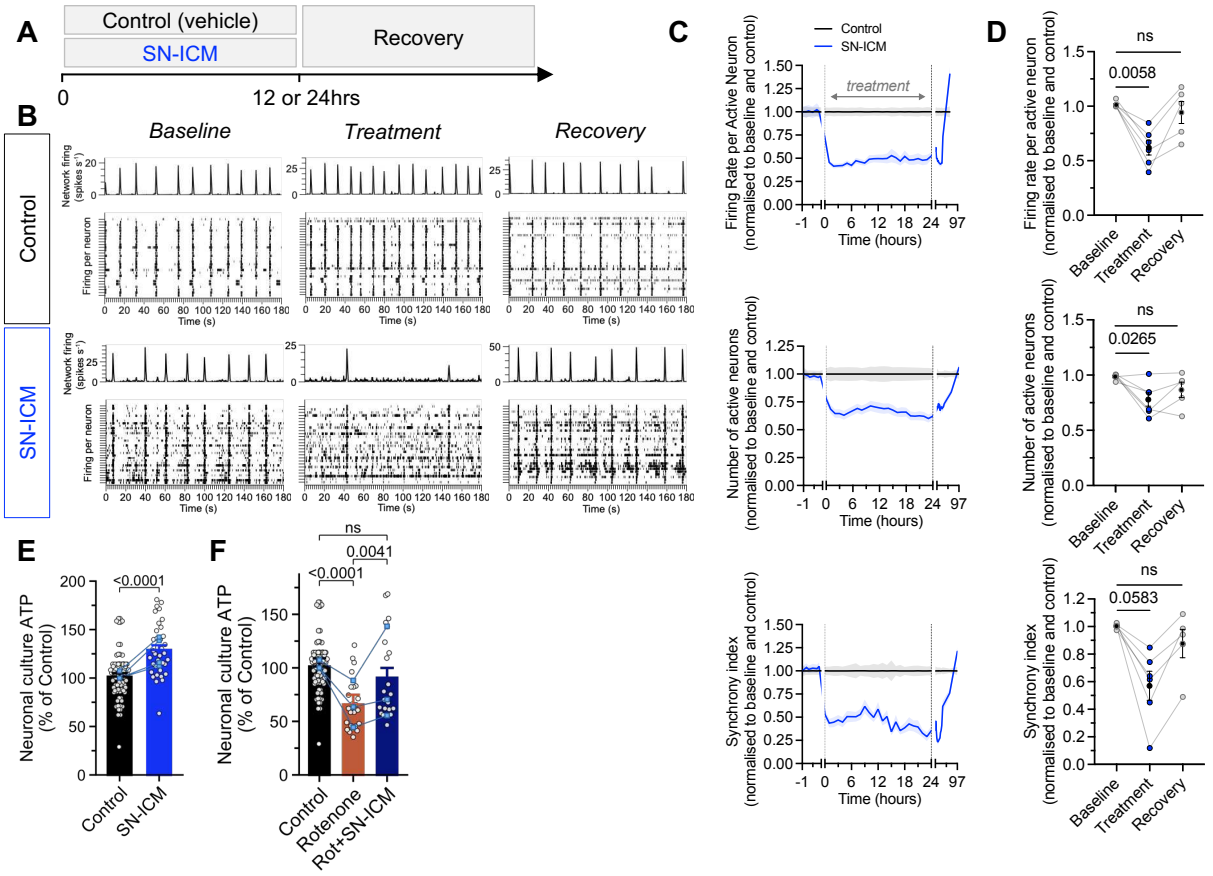


Figure 5. Substantia nigra-targeted ICMs reduce the electrical activity of human midbrain neurons and enhance ATP levels.

(**A**) Schematic depicting the treatment and recovery timeline for exposure of midbrain neural cultures to the SN-ICM cocktail (10 μM fisetin, 10 μM ML297, 100 nM α-conotoxin PIA, 100 nM α-conotoxin MII). (**B**) Representative 180s raster plots depicting action potential firing of individual neurons before, during and after exposure to the SN-ICM cocktail or vehicle control (0.13% DMSO). (**C**) Time-series graphs showing neuronal electrical activity before, during and after 24h of SN-ICM exposure, measured as the number of active neurons per well (>5 spikes per minute), firing rate of active neurons and synchrony index per well. Lines depict the mean of 36 wells from three independent MEA plates, and shaded areas indicate ± SEM. (**D**) Bar graphs summarise firing rate of active neurons, number of active neurons and synchrony index before treatment, during SN-ICM exposure and after recovery. Data represent n = 6 independent neural differentiations, each averaging 9-47 technical replicates. Data were first normalised to the average of six baseline recordings, and then to the average of the control recordings for each independent neural differentiation. Statistical significance determined using a ratio paired t-test. (**E**) ATP levels measured from lysates of cultures exposed to vehicle control or the SN-ICM cocktail for 24 h. Bars represent mean ± SEM. Data were normalised to the mean of the control condition (n = 4 independent neural differentiations). (**F**) ATP levels measured from lysates of cultures exposed for 24 h to vehicle control, rotenone at the concentration corresponding to a 50% reduction in ATP levels for each neural differentiation (IC50), or co-exposure to rotenone and the SN-ICM cocktail. Bars represent mean ± SEM. Data were normalised to the mean of the vehicle control (n = 3 independent neural differentiations). Control data are the same as in 5E minus one neural differentiation. (**E-F**) White circles represent individual well replicates, and blue squares with blue paired lines represent means per independent neural differentiation. Statistical significance was determined using linear mixed-effects models, as described in the Methods. See also Supplementary Figures S4 and S5.

Fig 6. Generic ion channel modulators are protective against ROS-mediated neurotoxicity and rotenone-mediated lysosomal dysfunction.

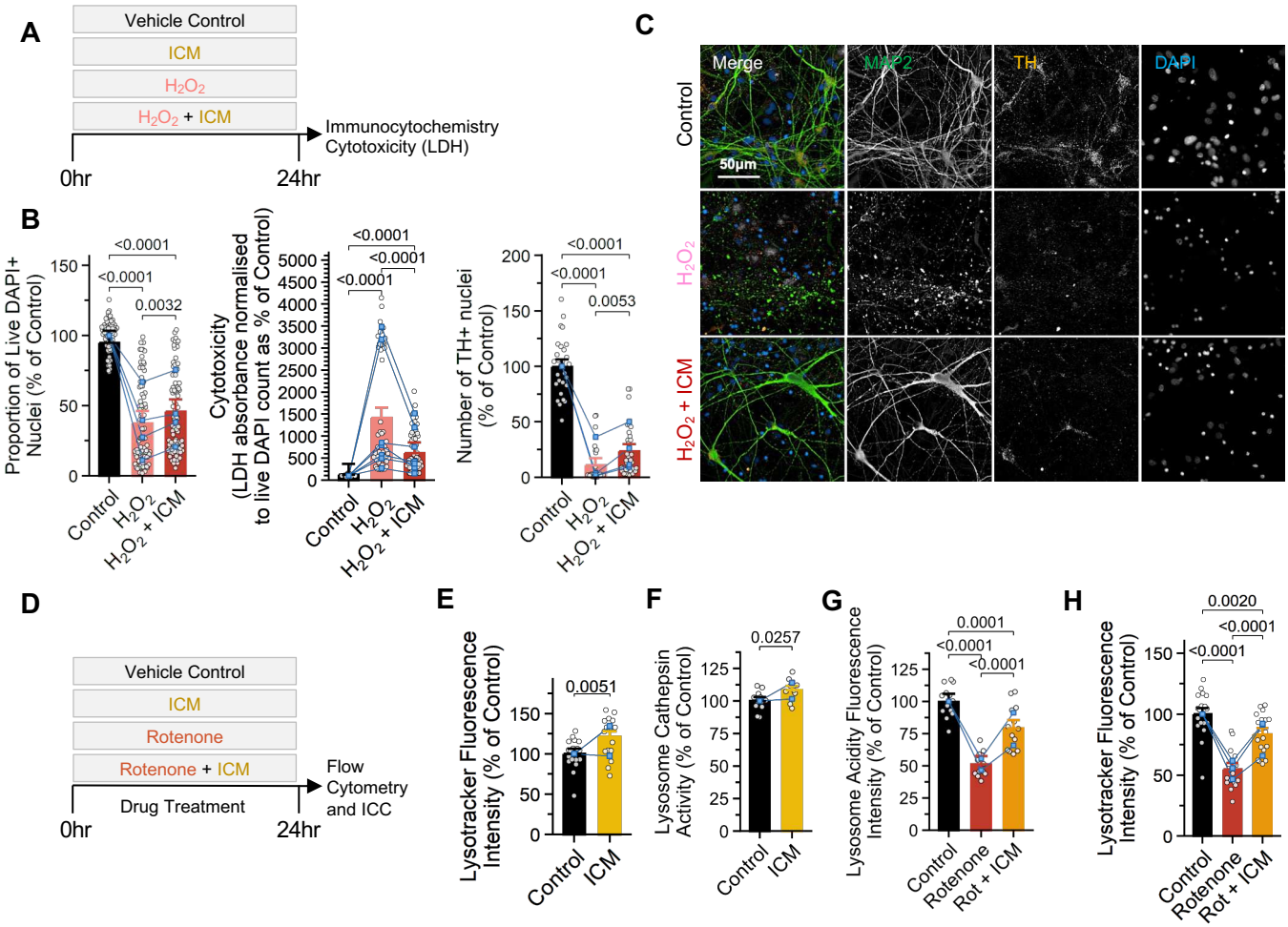


Figure 6. Generic ion channel modulators are protective against ROS-mediated neurotoxicity and rotenone-mediated lysosomal dysfunction.

(**A**) Schematic depicting the treatment timeline for exposure of midbrain neural cultures to ICMs and H_2O_2. (**B**) Biological replicates (n = 4-7) in B reflect H9-derived midbrain patterned neural cultures and pooled healthy patient-derived midbrain patterned neural cultures (villages; see Supplementary Figure S6D-E; Healthy village data in 6B are also shown in S6E). Neurodegeneration measured as the number of DAPI+ nuclei, lactate dehydrogenase (LDH) absorbance, and number of TH+ nuclei per well in cultures exposed to the ICM cocktail and either 500 µM, 1 mM or 1.5 mM H_2O_2 for 24 h. Bars represent mean ± SEM normalised to control. (**C**) Representative confocal images. DAPI-labelled nuclei are shown in blue. Antibody labelling shows neurons and dendrites (MAP2, green) and dopaminergic neurons (TH, orange). (**D**) Schematic depicting the treatment timeline for exposure to the ICM cocktail and rotenone. (**E–H**) Flow-cytometric analysis of LysoTracker Red or Magic Red fluorescence intensity per cell in cultures exposed to ICMs and rotenone (Rot) for 24 h. Bars represent mean ± SEM. Control data for E and G are the same, and control data for F and H are the same. (**B, E–H**) White circles represent individual well replicates, and blue squares with blue paired lines represent means per independent neural differentiation (n = 2-7). Statistical significance was determined using linear mixed-effects models, as described in the Methods. See also Supplementary Figures S6 and S7.

Fig 7. PARK2 mutations impair dopaminergic neurons and exacerbate vulnerability to oxidative stress in human midbrain cultures

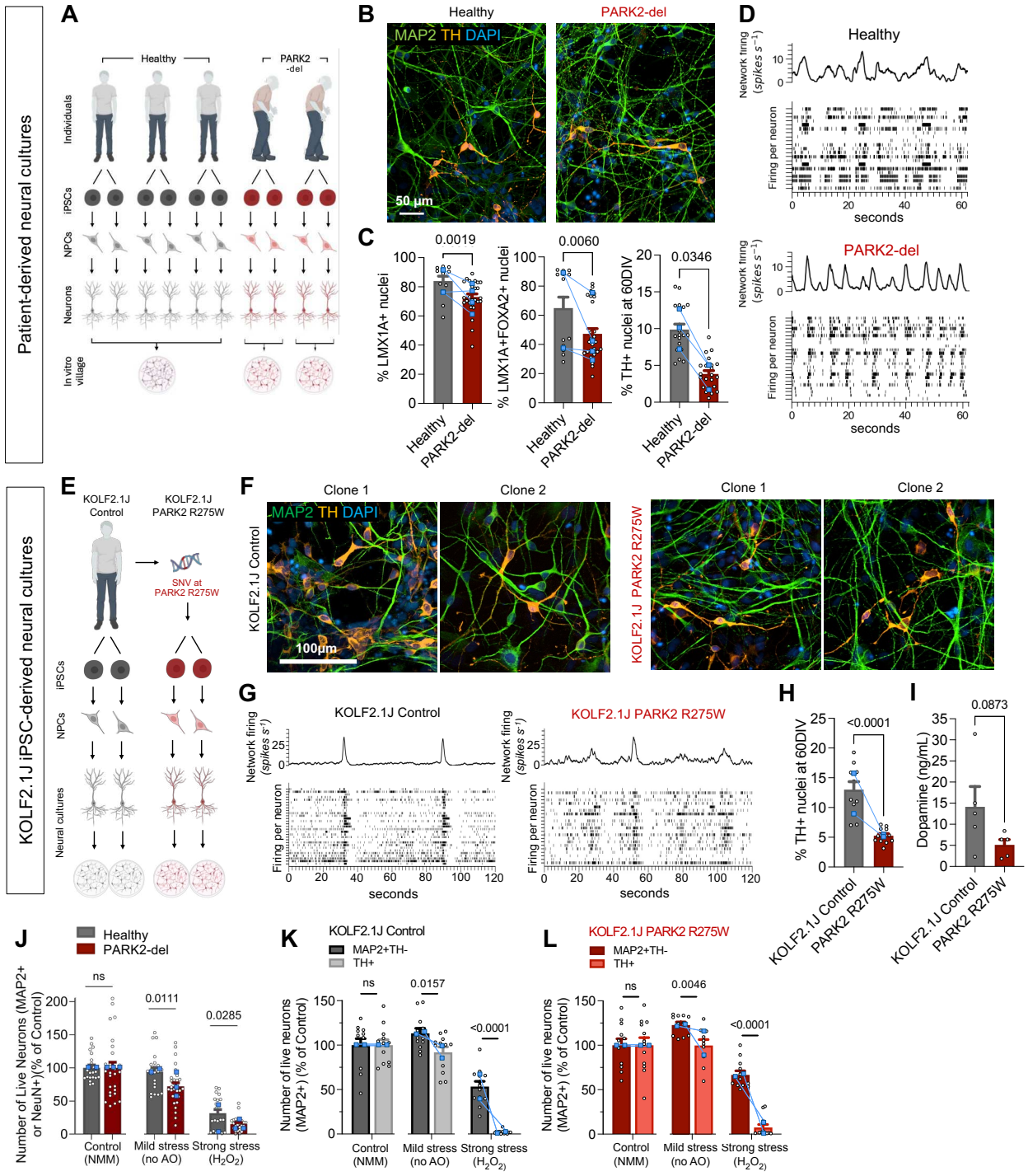


Figure 7. PARK2 mutations impair dopaminergic neurons and exacerbate vulnerability to oxidative stress in human midbrain cultures.

(**A**) Schematic of the patient-derived in vitro neural model. Six iPSC clones from three healthy individuals and four iPSC clones from two Parkinson's disease patients carrying PARK2 mutations were induced toward midbrain dopaminergic neurons. Healthy donor lines and PD patient clones were each combined into pooled "village" cultures and matured for 60 days in BrainPhys medium with supplements (NMM) before 24h exposure to ICMs and/or 500 μM H_2O_2. (**B**) Representative confocal images of patient-derived PARK2-mutant neural cultures. DAPI-labelled nuclei are shown in blue. Antibody labelling shows neurons and dendrites (MAP2, green) and dopaminergic neurons (TH, orange). (**C**) Dopaminergic patterning shown as the proportion of cells expressing LMX1A, FOXA2, and TH in control and PARK2-mutant village cultures. (**D**) Representative 60s raster plots depicting action potential firing of individual neurons in control and PARK2-mutant village cultures. Associated line graphs indicate firing density within synchronous network events. (**E**) Schematic of the isogenic in vitro neuronal model. Two iPSC clones from the KOLF2.1J control line and two iPSC clones from the KOLF2.1J PARK2 R275W SNV/SNV line were induced toward midbrain dopaminergic neurons and cultured in NMM for 60 days before experiments. (**F**) Representative confocal images of isogenic PARK2-mutant neural cultures. DAPI-labelled nuclei are shown in blue. Antibody labelling shows neurons and dendrites (MAP2, green) and dopaminergic neurons (TH, orange). (**G**) Representative 60s raster plots depicting action potential firing of individual neurons in isogenic control and PARK2-mutant cultures. (**H**) Proportion of TH-expressing nuclei in isogenic control and PARK2-mutant neural cultures. (**I**) Extracellular dopamine levels in isogenic control and PARK2-mutant neural cultures. White circles represent individual well replicates from one neural differentiation. Bars represent mean ± SEM. Statistical significance was determined using Mann-Whitney U Test. **(J-L)** Proportion of live neurons, defined as MAP2+ or NeuN+ nuclei, following antioxidant deprivation or exposure to 500 μM H_2O_2. (**C, H, J-L**) White circles represent individual well replicates, and blue squares with blue paired lines represent means per independent neural differentiation (n = 2-4). Bars represent mean ± SEM. Statistical significance was determined using linear mixed-effects models, as described in the Methods. See also Supplementary Figure S8.

Fig 8. Lowering neuronal electrical activity confers neuroprotection to PARK2-mutant human neural cultures

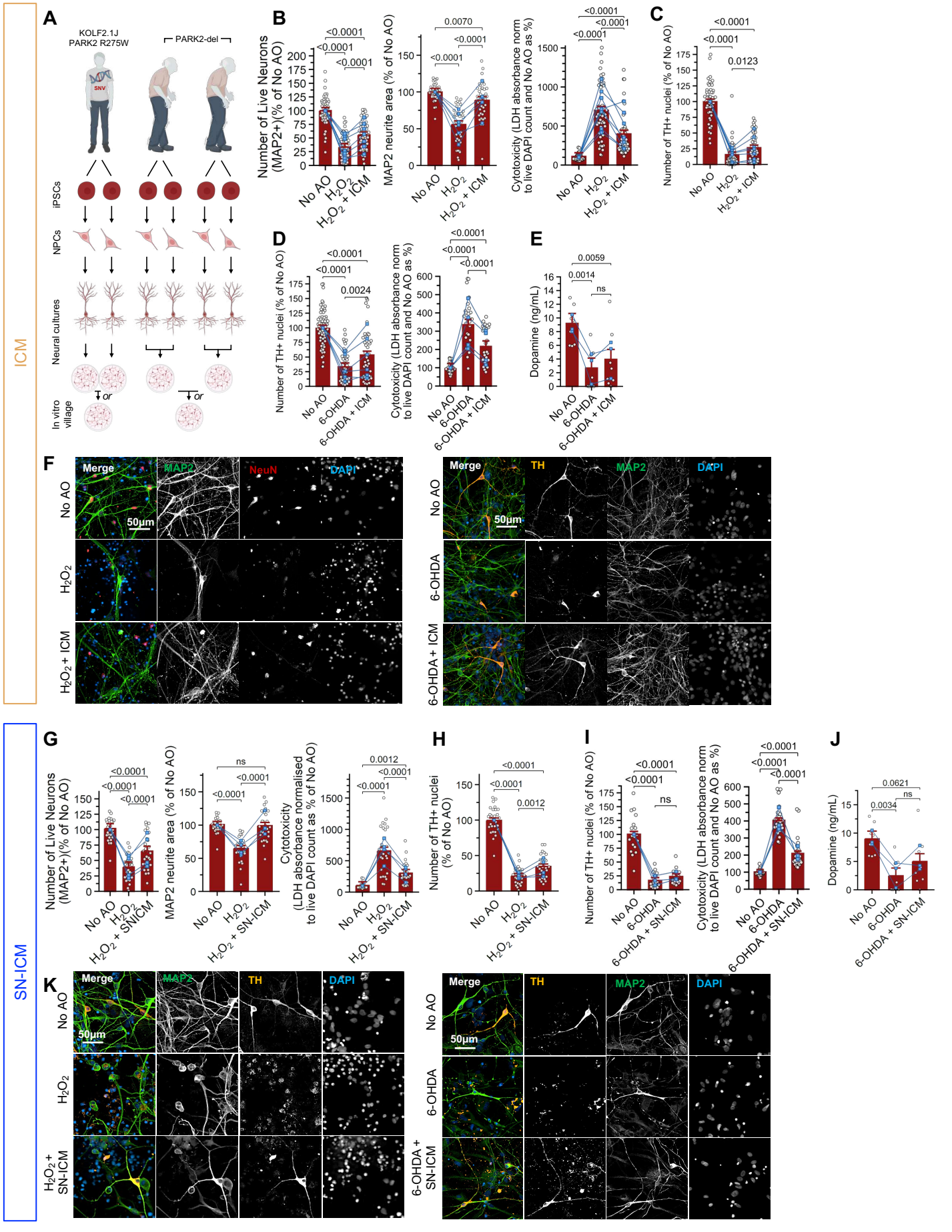


Figure 8. Lowering neuronal electrical activity confers neuroprotection to PARK2-mutant human neural cultures.

(**A**) Experimental overview of PARK2-mutant neural cultures. Two iPSC clones per line from the PARK2 R275W SNV/SNV isogenic model and from patient-derived PARK2-del lines, including a PARK2 heterozygous deletion at exons 3-5 and a PARK2-ex2del/c.202_203delAG mutation, were induced toward midbrain dopaminergic neurons. PARK2 R275W neural cultures were maintained either separately or as pooled cultures. PARK2-del patient cultures were maintained either separately, with clones pooled per patient, or combined as pooled cultures containing all four clones from the two patients. Cultures were pooled 14 days after neural differentiation in the plating process (see Methods). Cultures were matured for 60-120 days in NMM before 24h exposure to the indicated compounds. (**B**) Neurodegeneration measured as the number of live neurons, defined as MAP2+ or NeuN+ nuclei, MAP2+ neurite area, and LDH absorbance following exposure to ICMs and/or 500 µM H_2O_2. (**C**) Dopaminergic neurodegeneration measured as the number of neurons expressing TH per well and the number of TH+ nuclei with neurites following exposure to ICMs and/or 500 µM H_2O_2. (**D**) Dopaminergic neurodegeneration measured as the number of TH-expressing neurons and LDH absorbance following exposure to ICMs and/or 140-280 µM 6-hydroxydopamine (6-OHDA). (**E**) Culture medium dopamine levels measured by ELISA following exposure to ICMs and/or 6-OHDA. (**F**) Representative confocal images following exposure to H_2O_2, 6-OHDA and/or ICMs. Antibody labelling shows neurons and dendrites (MAP2, green), dopaminergic neurons (TH, orange) and/or neuronal nuclei (NeuN, red). DAPI-labelled nuclei are shown in blue. (**G**) Neurodegeneration measured as the number of live neurons, defined as MAP2+ or NeuN+ nuclei, MAP2+ neurite area, and LDH absorbance following exposure to the SN-ICM cocktail and/or 500 µM H_2O_2. (**H**) Dopaminergic neurodegeneration measured as the number of neurons expressing TH per well following exposure to the SN-ICM cocktail and/or 500 µM H_2O_2. (**I**) Dopaminergic neurodegeneration measured as the number of neurons expressing TH and LDH absorbance following exposure to the SN-ICM cocktail and/or 140-280 µM 6-OHDA. **(J)** Culture medium dopamine levels measured by ELISA following exposure to SN-ICMs and/or 6-OHDA. (**B-E, G–J**) Data are normalised as a percentage of the antioxidant-removal control condition (No AO). White circles represent individual well replicates, and blue squares with blue paired lines represent means per independent neural differentiation (n = 3-8). Bars represent mean **±** SEM. Statistical significance was determined using linear mixed-effects models, as described in the Methods. (**K**) Representative confocal images following exposure to 500 µM H_2O_2, 140-280 µM 6-OHDA and/or the SN-ICM cocktail. Antibody labelling shows neurons and dendrites (MAP2, green), dopaminergic neurons (TH, orange) and/or neuronal nuclei (NeuN, red). DAPI-labelled nuclei are shown in blue. See also Supplementary Figures S9 and S10.

Table 1. Ion channel modulators and cocktails

Pharmacological agents used to modulate neuronal electrical activity. The Table lists each compound's mechanism, target, function and potential off-target effects. The excitation or inhibition column denotes the intrinsic role of the target channel; the channel activity column denotes the effect of the modulator on that channel. AMPA, α-amino-3-hydroxy-5-methyl-4-isoxazolepropionic acid; GIRK, G protein-coupled inwardly rectifying potassium channel; GluK, kainate receptor subunit; GluN, NMDA receptor subunit; GluR, AMPA receptor subunit; HCN, hyperpolarisation-activated cyclic nucleotide-gated channel; Kir, inwardly rectifying potassium channel; nAChR, nicotinic acetylcholine receptor; Nav, voltage-gated sodium channel; NMDA, N-methyl-D-aspartate; P2X7, P2X purinoceptor 7.

Cocktail	Ion Channel Modulator	Description	Target	Target Channel	Channel Group	Channel Function	Excitation or Inhibition	Channel Activity	Potential off-target effects
Ion channel modulator (ICM) cocktail	Tetrodotoxin	Neurotoxin that blocks voltage gated sodium channels, preventing depolarisation.	Nav1.x	Voltage-gated sodium channel	Voltage-gated sodium channels	Cause cellular depolarisation for action potential firing	Excitation	Decrease	All sodium channels
	NBQX (2,3-dioxo-6-nitro-7-sulfamoyl-benzo[f]quinoxaline)	AMPA and Kainate receptor antagonist.	GluRX	AMPA receptors	AMPA receptors	Synaptic plasticity and excitatory neurotransmission	Excitation	Decrease	All AMPA receptors, Kainate receptors
	APV ((2*R*)-amino-5-phosphonovaleric acid)	Selective NMDA receptor antagonist	GluNX	NMDA receptors	NMDA receptors	Learning, memory and synaptic plasticity	Excitation	Decrease	All NMDA receptors
Substantia nigra-targeted ICM (SN-ICM) cocktail	α-conotoxin-PIA	Blocks nicotinic receptors containing α6 and α3 subunits	CHRNA6	Common: $\alpha_6\beta_3$* (* = additional subunit)	Nicotinic acetylcholine receptors	Cell depolarisation, neurotransmitter release	Excitation	Decrease	α_3 containing receptors
	α-conotoxin-MII	Potent and selective antagonist of a3b2 and b3 containing nAChRs	CHRNB3	Common: $\alpha_6\beta_3$* (* = additional subunit)	Nicotinic acetylcholine receptors	Cell depolarisation, neurotransmitter release	Excitation	Decrease	$\alpha_6\beta_2$*containing receptors
	ML297	Brain penetrant, selective Kir3.1/Kir3.2 (GIRK1/GIRK2) activator. Unable to activate homomeric GIRK2 channels but activates GIRK1/GIRK2 channels.	KCNJ6	Kir3.2 (GIRK2)	Inwardly rectifying potassium channels	Resting membrane potential regulation and modulates cell excitability	Inhibition	Increase	GIRK1
	Fisetin	Partial agonist of HCN2 channels	HCN2	HCN2	Cyclic nucleotide gated cation channels	Control neuronal excitability, oscillations and pacemaking	Excitation	Increase	Inhibits proinflammatory cytokine activity
Not in cocktails	Dihydro-β-erythroidine hydrobromide	Competitive nicotinic acetylcholine receptor antagonist for α4 receptor subunit.	CHRNB3, CHRNA4, CHRNA6	Common: $\alpha_6\beta_3$* (* = additional subunit) & a4b2	Nicotinic acetylcholine receptors	Cell depolarisation, neurotransmitter release	Excitation	Decrease	Neuronal nicotinic receptors
	VU0529331	Modestly selective drug that targets non-GIRK1 containing GIRK channels.	KCNJ6	Kir3.2 (GIRK2)	Inwardly rectifying potassium channels	Resting membrane potential regulation and modulates cell excitability	Inhibition	Increase	Channels with GIRK4
	UBP310	Orthosteric antagonist for the GluK1 subunit of kainate receptors.	GRIK1	GluK1	Kainate receptors	Excitatory synaptic transmission	Excitation	Decrease	N/A
	UBP302	A highly selective GluK1 subunit inhibitor, active enantiomer of UBP296.	GRIK1	GluK1	Kainate receptors	Excitatory synaptic transmission	Excitation	Decrease	N/A
	Brilliant Blue G	Non-competitive P2X7 antagonist that inhibits initial cationic flux through P2X7 receptors.	P2RX7	P2X7	Purinergic receptors	Mediate excitatory neurotransmission	Excitation	Decrease	N/A

Supplementary Files

This is a list of supplementary files associated with this preprint. Click to download.

- ePharmSupplementaryFiguresV11compressed.pdf
- ePharmAppendixMainFiguresNestedPlotsV1.pdf